

Deformable porous media saturated by three immiscible fluids: constitutive modeling and simulations of injection and imbibition tests

Alessandro Gajo · Francesco Cecinato · Benjamin Loret

Abstract A number of environmental and petroleum engineering applications involve the co-existence of three non miscible fluids. In this work, the basic constitutive relations and computational schemes are developed in order to simulate fluid injection and imbibition processes in a deformable rock through the finite element method. For this purpose, the following ingredients are worked out: (i) simple, but general formulas for the effective saturations; (ii) constitutive expressions for the relative permeabilities of water, oil and gas in terms of effective saturations; and (iii) constitutive capillary pressure relationships. These ingredients are introduced in a domestic finite element code where the primary variables are the solid displacement vector and the three fluid pressures. Given the abundance of experimental data in the petroleum engineering field, the whole framework is firstly tested by simulating gas injection into a rock core sample initially saturated by water and oil. Sensitivity analyses are performed upon varying key constitutive, loading and numerical parameters, to assess the physical and computational outputs of the proposed framework. Particular attention is given to the influence on the model outputs of the different expressions defining relative permeabilities. Simulations of water-alternated-gas injection and of counter-current water imbibition tests are also performed, to establish the reliability of the proposed constitutive and computational framework.

Keywords Immiscible fluids · Capillary pressure · Relative Permeability · Gas injection · Imbibition

1 Introduction

The co-existence of three non miscible fluids, typically water, a gaseous and an oily (or other non-aqueous) phase, is typical of several environmental processes, such as soil decontamination, and of enhanced hydrocarbon recovery processes, such as gas or steam injection and water alternating gas injection. In such cases, three-phase modeling is required. The relative wettability of the three fluids is known to influence significantly the macroscopic properties that govern multi-phase flow, like capillary pressures and relative permeabilities. Due to the relatively wide availability of published data in the hydrocarbon engineering field, the three fluids considered in this work are water, gas and oil, however the modelling framework described here is general enough to be applied to many other problems in geo-energy (e.g. CO₂ sequestration) and environmental engineering (e.g. air sparging for site remediation).

In a water-wet rock, water is more wetting than oil which is more wetting than gas. The contact angle between water and oil is smaller than 90°, oil is spreading spontaneously, and water keeps preferentially in contact with the rock matrix. Consequently, small pores contain mostly water, oil may invade intermediate and large pores and gas is restricted to the middle of large pores. This configuration motivates the water oil capillary pressure $p_o - p_w$ to be a function of the sole oil saturation and the oil gas capillary pressure $p_g - p_o$ to be a function of the sole gas saturation (e.g. see Helland and Skjæveland [2004]),

$$p_o - p_w = p_{cow}(S_o), \quad p_g - p_o = p_{cgo}(S_g). \quad (1.1)$$

Alessandro Gajo: Università di Trento, DICAM, Via Mesiano 77, 38123 Trento, Italy · Francesco Cecinato: Università di Trento, DICAM, Via Mesiano 77, 38123 Trento, Italy. Tel.: +39 0461 282585. E-mail: francesco.cecinato@unitn.it · Benjamin Loret: Université de Grenoble, Laboratoire 3SR, 38041 Grenoble Cedex 9, France

In a three-phase context, the above expressions need to be upgraded, to meet certain consistency conditions along the edges of the saturation triangle (ternary diagram representing the fluid saturations, see Section 2). It should be noted that in eqns (1.1), reference is made to effective saturations \underline{S}_k , $k = w, o, g$ which account for the irreducible saturations. The problem of conceiving a simple and flexible definition for effective saturations is not a trivial task in the presence of three non miscible fluids, and is addressed in Section 2.

For weakly oil wet rocks, oil is more wetting than water, which is more wetting than gas. The order of the two latter fluids is reverted for a strongly oil wet rock, and the pore occupancy of each fluid is modified accordingly. Considering standard wettability, the pressure difference between the least wetting and the most wetting fluid is always positive or zero. On the other hand, for mixed wettability, this pressure difference is positive at high saturation of the least wetting phase, and negative at high saturation of the most wetting phase (e.g., see Bradford and Leij [1996]).

The order of wettability has quantitative consequences also on relative permeabilities. In fact, the relative permeability to water is larger for oil-wet systems than for water-wet systems, and the opposite applies to the relative permeability to oil (see Anderson [1987], Fig. 2 therein).

A simplification can be introduced by assuming the relative permeability of both the most wetting and least wetting fluid to depend only on their respective effective saturation, while the relative permeability of the intermediate wetting fluid can be set to depend on both effective saturations of the other fluids. Namely, for a water wet rock (Corey et al. [1956]),

$$k_{rw} = k_{rw}(\underline{S}_w), \quad k_{ro} = k_{ro}(\underline{S}_w, \underline{S}_g), \quad k_{rg} = k_{rg}(\underline{S}_g). \quad (1.2)$$

While the above constitutive assumptions have been criticized by some authors for their lack of accuracy in reproducing available experimental data (e.g. Delshad and Pope [1989]), nevertheless they have been shown to roughly agree with the core flooding experiments on water wet sandstone by Alizadeh and Piri [2013], and with the experimental results discussed in a recent review of Egermann et al. [2013].

Typically, the extent of pore occupancy by water, oil and gas, as well as capillary pressures and relative permeabilities, are all path dependent, i.e. depending on whether drainage or imbibition occurs, Standing [1975], Hustad [2002], and Alizadeh and Piri [2013]. However, any hysteresis displayed by the relative permeability and capillary pressure paths is neglected for simplicity. Still, expressing the relative permeability of water as a function of water saturation only, eqn (1.2)₁, independently of the saturation path, agrees satisfactorily with the experiments reported by Grivot et al. [1995], Moulu et al. [1995], and Weifeng et al. [2012]. Moreover, emphasis is laid on water wet rocks. Since wettability depends on both the chemical composition of the fluids and on the mineralogy of the geomaterial at hand, the present developments should be considered more relevant to materials like coal, silicate rocks and sandstones, that are typically water wet, rather than on quartz-based and carbonate rocks, which are mostly oil wet.

A number of efforts have been made in the literature to address the problem of three immiscible fluid flow in porous media. Three-phase flow models are usually obtained based on two-phase models. Two alternative approaches have been proposed (e.g. see Morel-Seytoux [1973], Binning and Celia [1999]), either considering the individual mass balance of each phase (typically used in hydrology studies), or manipulating the mass balance equations to obtain a global fluid pressure and a total flux (so-called fractional flow approach, typically used in petroleum engineering). The latter approach is more widespread (recent contributions include Chen [2000] and Amiri et al. [2014]), however, it typically implies the water-oil capillary pressure to be expressed as a function of water saturation only, whereas the oil-gas capillary pressure is expressed as a function of gas saturation only. This type of simplifying assumption (cf. Leverett & Lewis [1941]) brings about limitations in the relative permeability versus saturation relationships. Among the authors who proposed three-fluid formulations based on the individual mass balance, Forsyth and Shao [1991] still adopted Leverett & Lewis' [1941] simplifying assumption and neglected mechanical couplings; Pao et al. [2001] did consider the solid skeleton deformability, but did not provide detailed development for the constitutive equations relating saturations to capillary pressures and to relative permeabilities in a three-phase context; Yin et al. [2009] provided validation for two-phase flow only; and Mroginsky et al. [2010] assumed strongly simplified capillary pressure relationships.

In this work, a comprehensive framework based on the finite element method to simulate fluid injection/imbibition processes in deformable rocks saturated by three immiscible fluids is developed, based on the individual mass balance of each phase, without resorting to specific simplifications. The solid displacement vector and the three fluid pressures are used as primary variables. Thus, some additional algebraic effort is required to obtain the expressions of saturations as functions of pressures, as compared to a

pressure-saturation formulation. In fact, a pressure-saturation formulation suffers from standard pitfalls, such as the presence of constraints on the variables, and the onset of possible problems when dealing with highly heterogeneous media. However, the key differences between the two alternative schemes are expected to lie in the computational performance, which is explored in detail elsewhere (e.g. Gajo et al. [2016]). The proposed model is then numerically validated by simulating different types of core flooding experiments. It should be emphasized that, despite being based on a certain choice of constitutive assumptions, the framework presented here is expected to be able to accommodate extensions, such as accounting for the path-dependence of constitutive equations of relative permeabilities and capillary pressures, and being able to deal with mixed wet or oil wet rocks.

The paper is structured as follows. In Section 2, a set of simple, yet general and original, formulas to express the effective saturations of each fluid is described. In Section 3, constitutive expressions for the three relative permeabilities of water, oil and gas in terms of these effective saturations are proposed. Section 4 outlines the constitutive expressions of the capillary pressures in a water wet rock saturated by these three immiscible fluids. The above items are implemented in a domestic finite element code, considering the solid displacement vector and the three fluid pressures as primary variables. In Section 5, the above outlined framework is tested by simulating gas injection experiments in an elastic rock sample initially saturated by water and oil. The model sensitivity to different constitutive, loading and numerical parameters is explored, to assess the transport, mechanical and computational implications of the proposed framework. Further, several models of relative permeabilities are tested to assess the influence of the constitutive details on the numerical outputs. Water alternated gas injection tests (Section 5.4) and counter-current imbibition tests (Section 6) are finally simulated, as a further check of the reliability of the proposed constitutive and computational framework.

2 Effective saturations for a three-fluid phase porous medium

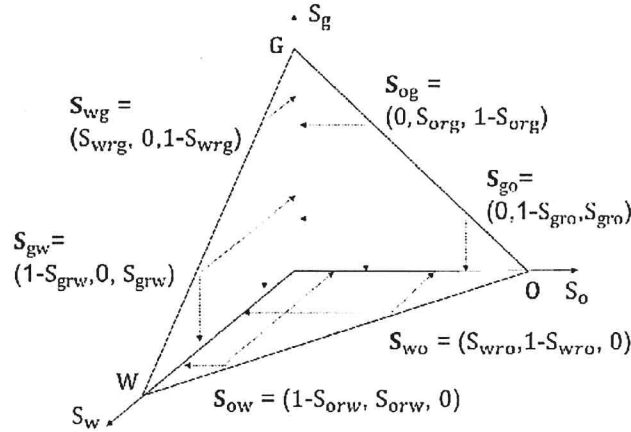


Fig. 2.1 The three-fluid saturations belong to the triangular domain $\mathcal{T} = \mathbf{WOG}$ defined in the cartesian axes (S_w, S_o, S_g) by the constraints $S_w + S_o + S_g = 1$, $S_w \geq 0$, $S_o \geq 0$, $S_g \geq 0$. Irreducible saturations further limit the ranges of the actual saturations. Notation: $S_{i,r,j}$ denotes the irreducible saturation of fluid i in presence of the sole fluid j .

Let us consider a fluid mixture $\mathcal{K}_f = \{w, o, g\}$ composed of three immiscible components, namely water w , oil o and gas g . To graphically represent the saturation domain, calling V_i the volume occupied by the component i and V_f the total fluid volume, cartesian coordinates can be considered in which the axes are the three-phase saturations,

$$S_i = \frac{V_i}{V_f}, \quad i = w, o, g, \quad (2.1)$$

that satisfy the constraint

$$S_w + S_o + S_g = 1. \quad (2.2)$$

In the cartesian space of axes (S_w, S_o, S_g) , the possible saturation values belong to a planar triangular domain $\mathcal{T} = \mathbf{WOG}$ defined by the apices \mathbf{W} , \mathbf{O} and \mathbf{G} corresponding to 100% water, oil and gas respectively,

see Fig. 2.1. A 2D representation of the same information can be given in the ternary diagrams shown in Fig. 2.2. In fact, the actual saturations range in the smaller irreducible domain $\mathcal{T}_r = \text{IJK}$ where the apices are obtained by joining the irreducible two-phase saturations, as shown in Fig. 2.2. Therefore, the positions of the irreducible saturations need to be input.

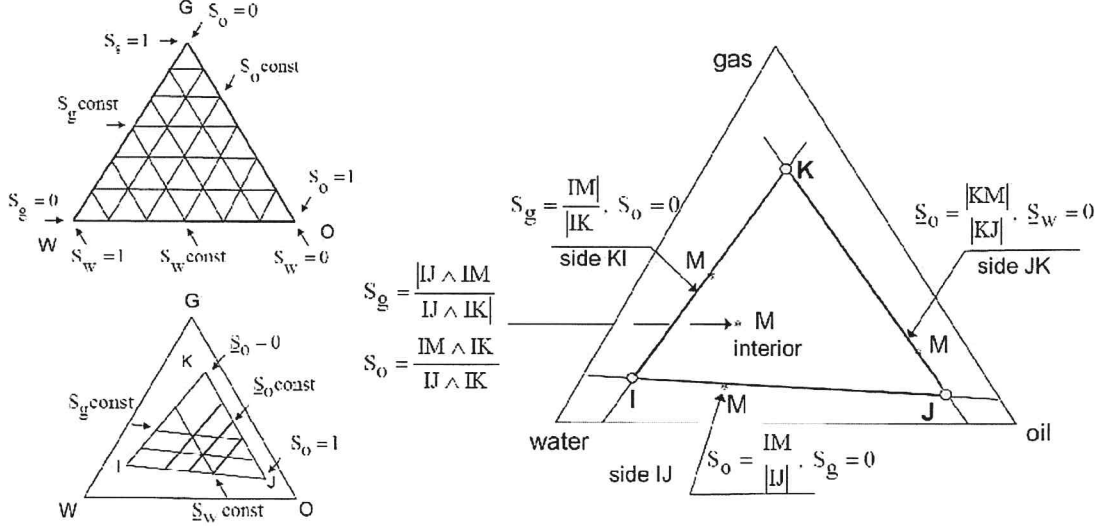


Fig. 2.2 Effective saturations within and along the edges of the irreducible triangle $\mathcal{T}_r = \text{IJK}$. The expressions are continuous in the neighborhood of the sides but they retrieve the familiar two-phase form *on* the edges. The third effective saturation is obtained by the condition that the three effective saturations sum to one.

With reference to Fig. 2.2, the effective saturation \underline{S}_w of water is equal to 1 at the apex I and vanishes on the opposite side JK of \mathcal{T}_r . The same rule applies to oil and gas. The three effective saturations sum to 1, they are linear functions of the effective saturations, and they can be expressed simply by the following vector products: if M is a current point of triangle \mathcal{T}_r ,

$$\underline{S}_w = \frac{|\text{JK} \wedge \text{JM}|}{|\text{JK} \wedge \text{JI}|}, \quad \underline{S}_o = \frac{|\text{IM} \wedge \text{IK}|}{|\text{IJ} \wedge \text{IK}|}, \quad \underline{S}_g = \frac{|\text{IJ} \wedge \text{IM}|}{|\text{IJ} \wedge \text{IK}|}. \quad (2.3)$$

The above linear map (2.3) represents an original formulation that, despite its simplicity, brings advantages over previously proposed expressions, being valid for arbitrary locations of the irreducible endpoints along each phase. The three denominators in (2.3) are equal to twice the area of the irreducible triangle \mathcal{T}_r . Further details and useful relations for effective saturations are reported in Appendix A.

Previous attempts in a three-fluid context, e.g. eqn (24) of Juanes and Patzek [2004], of the form $\underline{S}_i = (S_i - S_{ir}) / (1 - S_{wr} - S_{or} - S_{gr})$, typically sum to one but assume the sides of the irreducible triangle \mathcal{T}_r to be parallel to the triangle \mathcal{T} .

3 Relative permeabilities for a three-fluid phase porous medium

The relative permeability of each fluid is expected to depend on its pore occupancy. This dependence is known to be highly non linear even in a two fluid context, Anderson [1987]. The aim of this section is postulate algebraic expressions as simple as possible, yet in qualitative agreement with core analysis measurements. The consequences on the nature of the partial differential equations of mass balance have been addressed separately.

3.1 Constitutive equations of fluid transport

Flow of the fluid k through the porous skeleton is described by the standard form of Darcy's law, which provides the mass flux \mathbf{M}_k in terms of the pressure gradient,

$$\mathbf{M}_k \equiv n_k \rho_k (\mathbf{v}_k - \mathbf{v}_s) = -D_k (\nabla p_k - \rho_k \mathbf{g}), \quad D_k \equiv \rho_k k_{rk} \frac{k_{in}}{\eta_k}, \quad (3.1)$$

where \mathbf{v}_k and \mathbf{v}_s the velocities of fluid k and of the solids, respectively, ρ_k is the mass density of fluid k and \mathbf{g} the gravity vector. The intrinsic hydraulic permeability k_{in} [unit: m^2] is a property of the porous skeleton while the dynamic viscosity η_k [unit: $\text{Pa}\cdot\text{s}=\text{kg}/\text{m}\cdot\text{s}=10^3$ centipoise] (strongly temperature dependent for oil), the intrinsic mass density ρ_k [unit: kg/m^3] and volume fraction n_k pertain to the permeant fluid k . If the pore space is occupied by the sole fluid k , the relative permeability k_{rk} [unit: 1] is equal to 1; otherwise, it is smaller than 1 and depends on the saturations of the fluids (and flow history) in the pore space, as detailed below.

3.2 Three-phase relative permeabilities by weighting two-phase contributions

Following Hustad [2002], the relative permeability of fluid k is obtained by weighting its contributions in two of the two-phase systems by the partner effective saturations,

$$k_{rk} = \frac{k_{rki} \underline{S}_i + k_{rkj} \underline{S}_j}{\underline{S}_i + \underline{S}_j}, \quad i \neq j \neq k. \quad (3.2)$$

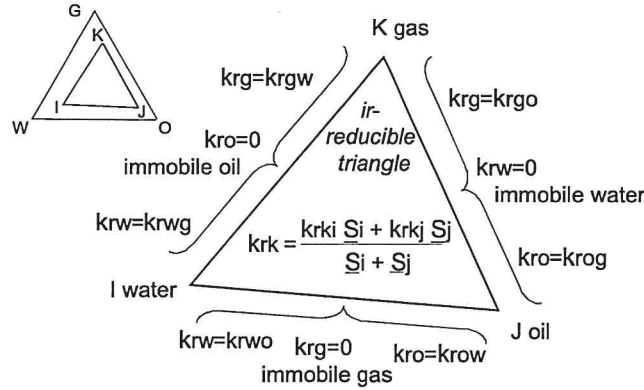


Fig. 3.1 The three-phase relative permeability of the fluid k is obtained by weighting its contributions k_{rki} and k_{rkj} on two of the two-phase subsystems by the effective saturations, eqn (3.2). With this weighting, the relative permeability to fluid k is equal to the two-phase relative permeability k_{rki} on the side ki adjacent to the apex k where $\underline{S}_j = 0$ and it vanishes on the opposite side ij of the irreducible triangle where $k_{rki} = k_{rkj} = 0$.

The above expression is illustrated in a schematic in Fig.3.1. For each two-phase system, the relative permeabilities can be described along the lines of Brooks and Corey's [1964] model:

$$\begin{aligned} \text{water/oil system, water wetting: } k_{rwo} &= \underline{S}_w^{2/\lambda+3}, & k_{row} &= \underline{S}_o^2 (1 - (1 - \underline{S}_o)^{2/\lambda+1}), \\ \text{oil/gas system, oil wetting: } k_{rog} &= \underline{S}_o^{2/\lambda+3}, & k_{rgo} &= \underline{S}_g^2 (1 - (1 - \underline{S}_g)^{2/\lambda+1}), \\ \text{water/gas system, water wetting: } k_{rwg} &= \underline{S}_w^{2/\lambda+3}, & k_{rgw} &= \underline{S}_g^2 (1 - (1 - \underline{S}_g)^{2/\lambda+1}), \end{aligned} \quad (3.3)$$

while, for an oil-wet rock, the relations of the water/oil system would be changed to

$$\text{water/oil system, oil wetting: } k_{row} = \underline{S}_o^{2/\lambda+3}, \quad k_{rwo} = \underline{S}_w^2 (1 - (1 - \underline{S}_w)^{2/\lambda+1}). \quad (3.4)$$

For a water wet system, the following more explicit expressions result from the insertion of (3.3) into the combination (3.2),

$$k_{rw} = \underline{S}_w^{2/\lambda+3}, \quad k_{ro} = \underline{S}_o^{2/\lambda+3} + \underline{S}_w \underline{S}_o^2 \left(\frac{1 - \underline{S}_o^{2/\lambda+1}}{1 - \underline{S}_o} - (1 - \underline{S}_o)^{2/\lambda} \right), \quad k_{rg} = \underline{S}_g^2 (1 - (1 - \underline{S}_g)^{2/\lambda+1}). \quad (3.5)$$

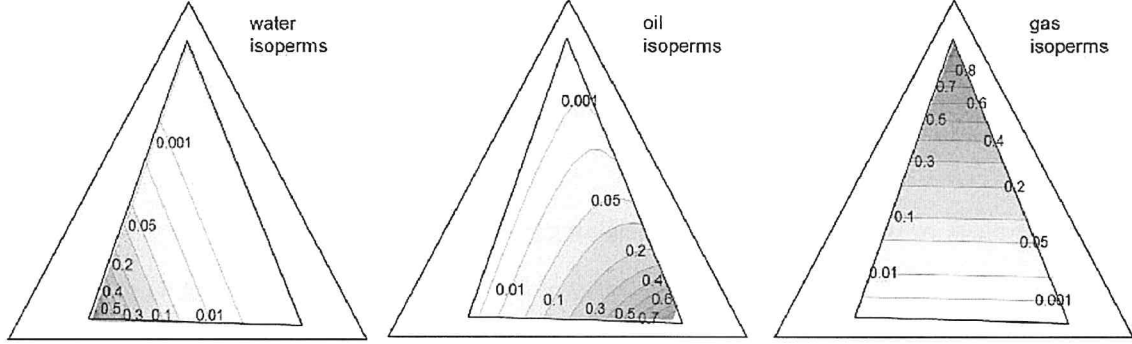


Fig. 3.2 Contours over the irreducible saturation triangle of the relative permeabilities to water, oil and gas for the weighted combination (3.2) based on the Brooks-Corey formulas (3.3) with a pore size distribution index $\lambda = 0.8$.

The relative permeability contours obtained with the above relations are displayed in Fig. 3.2 for a water wet system. While the contours of relative permeability to water k_{rw} and oil k_{rg} (Fig. 3.2a and 3.2c respectively) are parallel to the respective edges KJ and IK of the irreducible saturation triangle (Fig. 3.1), the contours of the relative permeability to oil k_{ro} (Fig. 3.2b) are concave with respect to the oil apex. These general patterns are in overall agreement with the literature review results over a number of sandstones and carbonates reported by Egermann et al. [2013].

In the simulations discussed in Sect. 5, the pore size distribution index λ is taken equal to 0.8. The pore size distribution index is large for uniform pore size and low for a scattered distribution, and $\lambda = 0.8$ corresponds to a rather scattered pore size distribution. Li [2004] proposed a relation between λ and the fractal dimension of the pore structure d_f , which is a measure of its heterogeneity, as $\lambda = 3 - d_f$. For a low pore size distribution, the permeability vs saturation curve of the wetting fluid appears ‘L-shaped’, i.e. it exhibits high curvature, while the permeability vs saturation curve of the non-wetting counterpart appears less incurvate: the two curves are definitely unsymmetrical with respect to each other (e.g., see Anderson [1987]). Increasing the value of the pore size distribution index progressively leads to a decrease of this asymmetry, and the two curves tend to depend on the effective saturation raised to the cube.

An alternative model, that might be viewed as a simplification of the Brooks-Corey relations, will be referred to as ‘symmetric formulation’, as the saturation vs permeability curves for the wetting and non wetting fluid are treated symmetrically; namely, in a two-fluid phase context,

$$k_{rij} = \underline{S}_i^\omega, \quad k_{rji} = \underline{S}_j^\omega. \quad (3.6)$$

For an exponent $\omega = 1$, the relative permeabilities vary linearly with effective saturation. A large exponent ω causes the relative permeability vs saturation curves to increase their curvature (i.e. to become more ‘L-shaped’) and gives rise to steep propagation fronts. If, in a three-phase context, either water or oil wetting, expressions (3.6) are used in the linear combination (3.2), they result in the relative permeabilities,

$$k_{rw} = \underline{S}_w^\omega, \quad k_{ro} = \underline{S}_o^\omega, \quad k_{rg} = \underline{S}_g^\omega. \quad (3.7)$$

The above expressions imply that, for any exponent ω , the contours of the three relative permeabilities are parallel to the edges of the irreducible saturation triangle.

3.3 Alternative three-fluid phase permeability models

As an alternative to the above illustrated approach to permeability modelling, three different existing models have been tested in our simulations. The first alternative is the so-called Stone model (Bell et al. [1986]), expressed as

$$\begin{aligned} k_{rw} &= 1.09 \underline{S}_w^{1.516687} - 0.09 \underline{S}_w^{4.5188}, \\ k_{ro} &= (1.19 (1 - \underline{S}_g)^{1.006} - 0.19 (1 - \underline{S}_g)^{1.024}) (1.95 (1 - \underline{S}_w)^{7.28} - 0.95 (1 - \underline{S}_w)^{10.284}), \\ k_{rg} &= 0.525 \underline{S}_g^{1.02} + 0.475 \underline{S}_g^{3.62}. \end{aligned} \quad (3.8)$$

The second alternative is the model of Juanes and Patzek [2004]:

$$k_{rw} = \underline{S}_w^2, \quad k_{ro} = \underline{S}_o (1 - \underline{S}_w) (1 - \underline{S}_g), \quad k_{rg} = \beta_g \underline{S}_g + (1 - \beta_g) \underline{S}_g^2. \quad (3.9)$$

The constraints $\beta_g > \eta_g / \sqrt{\eta_w \eta_o}$ and $\eta_o > \eta_w / 2$ should be enforced to ensure strict hyperbolicity, where the η 's represent the dynamic viscosities of the fluids. In fact, in the simulations shown in Sect. 5 $\beta_g = 2 \eta_g / \sqrt{\eta_w \eta_o}$ is assumed. With this setting, the resulting relative permeability values along the edges of the ternary diagrams are almost equal to the effective permeabilities raised to the square. Thus, the two-phase restriction of Juanes and Patzek's [2004] model yields similar results to the symmetric formulation (eqn 3.7) with $\omega = 2$.

The third alternative model examined considers a bundle of cylindrical capillary tubes, hereafter referred to as 'bundle' model (e.g., see Jackson and Blunt [2002]):

$$k_{rw} = \underline{S}_w^{5/3}, \quad k_{ro} = (1 - \underline{S}_g)^{5/3} - \underline{S}_w^{5/3}, \quad k_{rg} = 1 - (1 - \underline{S}_g)^{5/3}. \quad (3.10)$$

The resulting relative permeability vs saturation curves are 'L-shaped' along the edges of the irreducible saturation triangle, with upward concavity for both Juanes and Patzek's and the Stone model, while they exhibit downward concavity for the 'bundle' model.

To provide further insight into the specific nature of the different models that have been used, in Figs. 3.3-3.6 contours of relative permeability to water, oil and gas over the saturation triangle for all of the tested alternative relative permeability models are shown.

Similarly to the Brooks-Corey model, for all of the alternative models the contours of relative permeabilities to water k_{rw} and to gas k_{rg} are parallel to the respective edges KJ and IJ of the irreducible saturation triangle, as shown in Figs. 3.3-3.6. Also, the contours of relative permeability to oil k_{ro} are concave with respect to the oil apex for all models, except for the symmetric formulation that causes them to be parallel to edge IK (Fig. 3.5-b).

The three relative permeability expressions in the symmetric formulation with $\omega = 1$, eqn (3.7), and in the 'bundle' model, eqn (3.10), sum to one. This property, however, does not hold for all models. In fact, the sum of permeabilities should be strictly smaller than one, consistently implying that the fluid interactions hinder their seepage. The inequality reflects the experimental evidence that two-phase flows reduce considerably the relative permeability of the fluids. In other words, typically at mean saturations, the sum of the two relative permeabilities is much lower than 1 (e.g. Anderson [1987]). In a three-phase flow context, this phenomenon is exacerbated, as observed (e.g.) by Shahverdi et al. [2011]. As an example, let us consider a configuration where the fluids have identical (effective) saturation, i.e. 1/2 and 1/3 for two- and three-fluid phases respectively, and identical dynamic viscosity. In this configuration, according to the symmetric formulation, the sum of the two (or three) relative permeabilities is equal to $2^{1-\omega}$ (or $3^{1-\omega}$), that is for $\omega = 2$, to 1/2 and 1/3 for two- and three-fluid phases respectively. For the Brooks-Corey model with a large pore size distribution index, these numbers reduce to 1/4 and 1/9, respectively.

3.4 Remarks on relative permeability models

The five above discussed relative permeability models can be viewed as basic ingredients in this work; however, they should be considered as prototype models, since no fine tuning of parameters to fit specific datasets is carried out here. However, some limitations of these models can be highlighted based on literature observations. For example, it emerges that the above models are unsuitable to reproduce the fact that the saturation intervals over which the relative permeabilities to water and oil are non zero may be shifted with respect to one another (e.g., see Fig. 4.38 of Chalaturnyk [1996], and Suicmez et al. [2006]), which

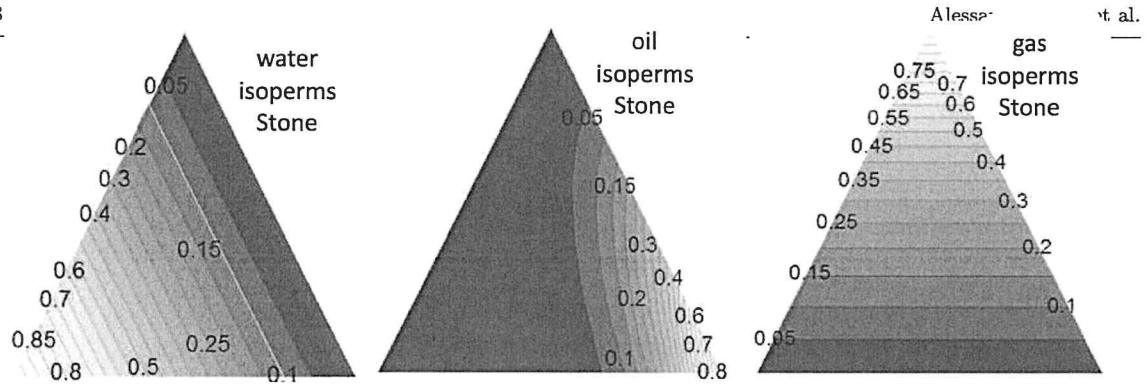


Fig. 3.3 Contours over the saturation triangle of the relative permeabilities to water, oil and gas based on the Stone model. Irreducible saturation was set to zero.

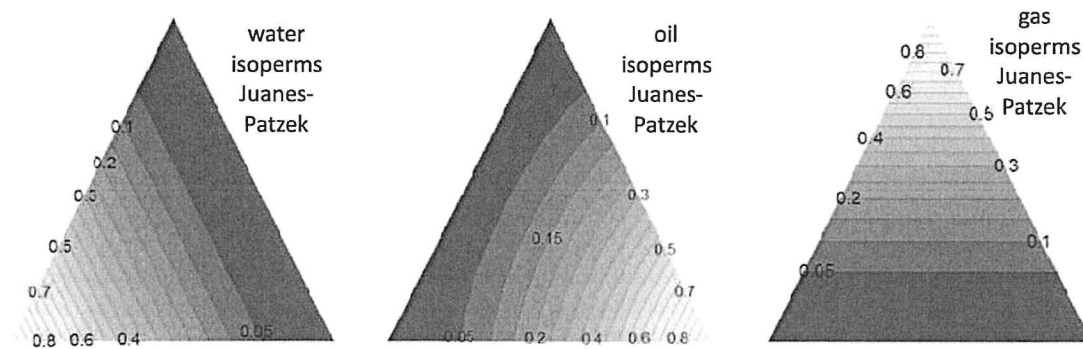


Fig. 3.4 Contours over the saturation triangle of the relative permeabilities to water, oil and gas based on the Juanes-Patzek model. Irreducible saturation was set to zero.

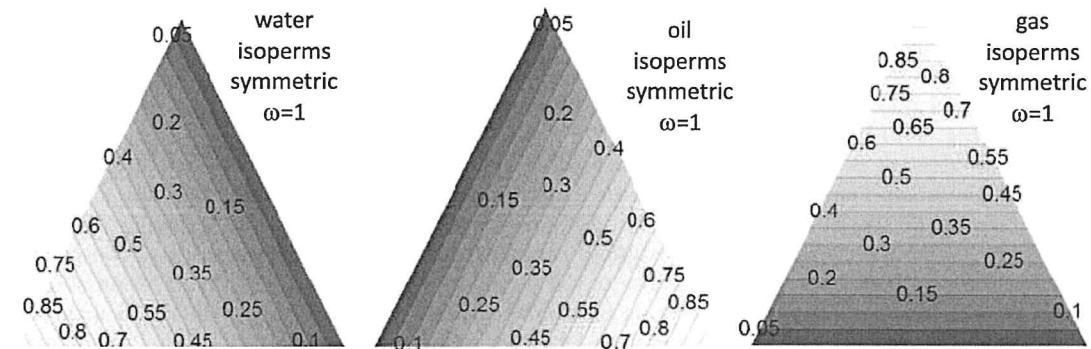


Fig. 3.5 Contours over the saturation triangle of the relative permeabilities to water, oil and gas based on the symmetric formulation with $\omega = 1$. Irreducible saturation was set to zero.

may especially occur in tight reservoirs. Another shortcoming of the permeability models at hand is that, in a two-fluid phase situation along the edges of the saturation triangle, they yield a maximum relative permeability equal to 1, at variance with (e.g.) the measurements reported by Anderson [1987] during imbibition of water wet rocks (cf. fig. 2 of Anderson [1987]).

From the mathematical point of view, the regime of the field equations of mass balance was checked for possible regions in the saturation space where hyperbolicity may be lost, along the lines of the analyses of Bell et al. [1986] and Juanes and Patzek [2004]. All relative permeability models described above were examined in this respect. When capillary forces are neglected, along the lines of Bell et al. [1986], the only model exhibiting a finite zone where hyperbolicity is lost is the Stone model. For all other models, hyperbolicity holds strictly, except possibly at certain isolated points where two wave-speeds are equal. On the other hand, accounting for capillary forces, as described by eqns (4.3) or (4.5) below, was numerically

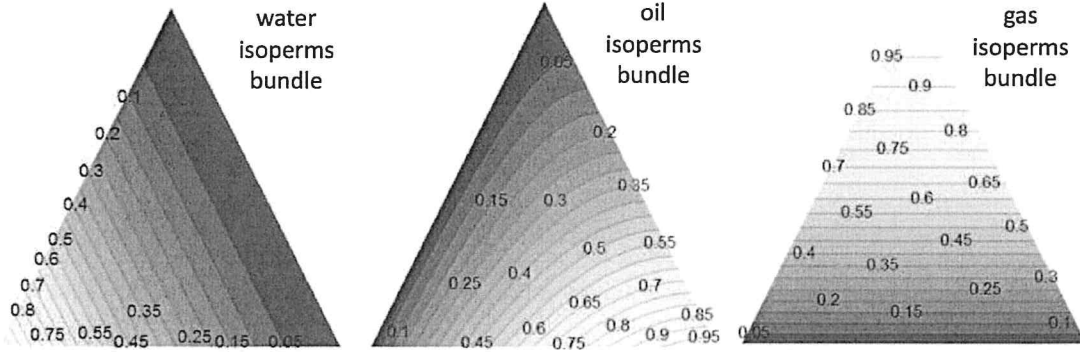


Fig. 3.6 Contours over the saturation triangle of the relative permeabilities to water, oil and gas based on the bundle model. Irreducible saturation was set to zero.

checked to enlarge the zone of loss of hyperbolicity for the Stone model, but did not change the hyperbolic nature of the other models.

Gas injection will be shown in Section 5 to give rise to the propagation of a gas saturation front at finite speed. Still, adopting the Stone model, the symmetric formulation with $\omega = 1$ or the ‘bundle’ model, such propagation speed is very large, and the propagation front is followed by a diffusion-like behavior. However, this feature cannot be generally ascribed to a hyperbolicity loss, since hyperbolicity was checked to hold for all models in the whole saturation triangle, with the sole exception of the Stone model.

4 Capillary pressures for a three-fluid phase porous medium

For the two-phase system ij , with j the wetting fluid, the capillary pressure $p_c = p_{cij} = p_i - p_j$ is positive, it is infinite for $\underline{S}_i = 1$, and it vanishes for $\underline{S}_i = 0$. Two expressions are routinely used. The smooth van Genuchten [1980] function,

$$\frac{p_c}{p_{c0}} = f(1 - \underline{S}_i) = \left((1 - \underline{S}_i)^{\frac{-1}{m}} - 1 \right)^{\frac{1}{n}}, \quad (4.1)$$

involves an exponent n , which satisfies the constraints $1 > m = 1 - 1/n > 0$ and a threshold (so-called ‘entry’) value of capillary pressure p_{c0} . The alternative Brooks-Corey relation,

$$\underline{S}_j = 1 - \underline{S}_i = \begin{cases} (p_{ie}/p_c)^\lambda, & p_c \geq p_{ie}; \\ 1, & 0 < p_c < p_{ie}, \end{cases} \quad (4.2)$$

is defined in terms of a single exponent as well, namely the pore size distribution index $\lambda \geq 0$ (introduced in Section 3.2). Increasing λ increases the curvature of the capillary pressure vs saturation plots. The Brooks-Corey relation, although simple, displays a discontinuous derivative at the entry value p_{ie} , which is prone to numerical problems.

In deriving three-phase capillary pressure relations, only the case of a water wet rock, where water is more wetting than oil which is more wetting than gas, is considered here. Two main approaches are possible. One may postulate three capillary pressure expressions. However, these expressions would need a priori to be corrected, because there are only two independent capillary pressures. In fact, the compatibility condition requires that $p_g - p_w = (p_g - p_o) + (p_o - p_w)$. A method to cope with this constraint was proposed by Hustad [2002]. An alternative approach consists in postulating two capillary pressures, and deduce the third one by virtue of the compatibility condition. In the following, the latter approach is adopted, due to its simplicity.

If used in a three-phase context, relation (4.1) implies the contours of the capillary pressure $p_i - p_j$ to be parallel to the jk side of the irreducible triangle. Instead, we propose here to adopt the following

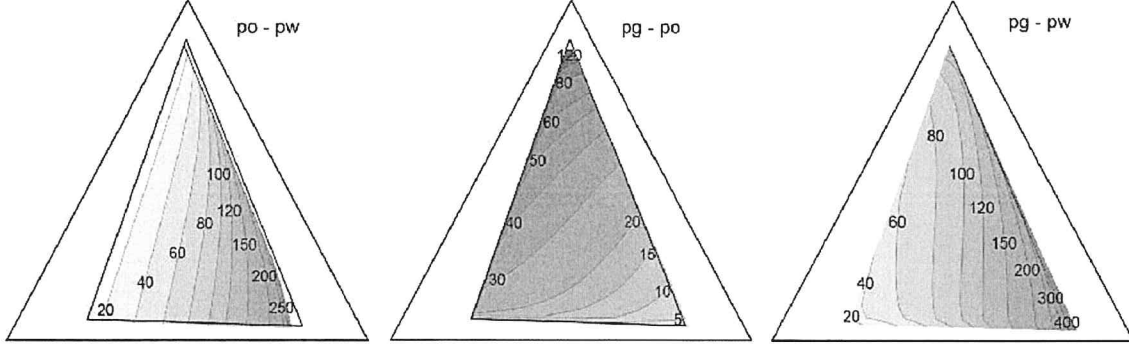


Fig. 4.1 Contours of the capillary pressures, expressed as (4.3), over the irreducible saturation triangle for a water wet rock [unit : kPa].

relations:

$$\begin{aligned}
 p_{cow} = p_o - p_w &= A \left((1 - \underline{S}_o)^{\frac{-1}{m}} - 1 \right)^{\frac{1}{n}} \left((1 - \underline{S}_o) \underline{S}_g + (1 - \underline{S}_g) \right) \\
 &\quad + B \left((\underline{S}_w)^{\frac{-1}{m}} - 1 \right)^{\frac{1}{n}} \underline{S}_o; \\
 p_{cgo} = p_g - p_o &= C \left((1 - \underline{S}_g)^{\frac{-1}{m}} - 1 \right)^{\frac{1}{n}} \left(1 - \underline{S}_o + 0.25 (1 - \underline{S}_w)^{0.1} \right) \\
 &\quad - A \left((1 - \underline{S}_o)^{\frac{-1}{m}} - 1 \right)^{\frac{1}{n}} (1 - \underline{S}_o) \underline{S}_g; \\
 p_{cgw} = p_g - p_w &= p_{cow} + p_{cgo}.
 \end{aligned} \tag{4.3}$$

In the above, $m = 1 - 1/n$, and exponent n and coefficients A , B , C are to be calibrated based on the available experimental results. In the applications discussed below, $n = 4$, and $A = 30$ kPa, $B = 100$ kPa and $C = 40$ kPa have been used. The above relationships are formulated to provide more realistic curves over the irreducible saturation triangle, Fig. 4.1. To better explain these relations, it is useful to rewrite them in a more formal way, indicating f as the van Genuchten function and a , b , c as other functions of the effective saturations:

$$\begin{aligned}
 p_o - p_w &= A f(1 - \underline{S}_o) c(\underline{S}_o, \underline{S}_g) + B f(\underline{S}_w) \underline{S}_o; \\
 p_g - p_o &= C f(1 - \underline{S}_g) a(\underline{S}_w, \underline{S}_o) - A f(1 - \underline{S}_o) b(\underline{S}_o, \underline{S}_g).
 \end{aligned} \tag{4.4}$$

In fact, in the first equation of (4.4) expressing the capillary pressure $p_o - p_w$, the first term $f(1 - \underline{S}_o)$ aims at reproducing the capillary pressure along the water-oil edge of the irreducible triangle, while the term $f(\underline{S}_w)$ induces an infinite capillary pressure along the oil-gas edge $\underline{S}_w = 0$. This second contribution vanishes on the water-gas edge where $\underline{S}_o = 0$, and so does the first contribution $f(1 - \underline{S}_o)$.

In the second equation of (4.4) expressing the capillary pressure $p_g - p_o$, the first term $f(1 - \underline{S}_g)$ aims at reproducing the capillary pressure along the oil-gas edge of the irreducible triangle while the term $f(1 - \underline{S}_o)$ induces a large capillary pressure near the oil apex which is mitigated by factor \underline{S}_g . So the capillary pressure vanishes along the water-oil edge $\underline{S}_g = 0$. Along the water-gas edge, the second term vanishes and the van Genuchten pattern of the capillary pressure $f(1 - \underline{S}_g)$ is mitigated by factor $a(\underline{S}_w, \underline{S}_o = 0)$.

On the water-gas edge ($\underline{S}_o = 0$), the capillary pressure $p_o - p_w$ vanishes so that $p_g - p_w$ is contributed by $p_g - p_o$, namely, by using the above coefficient settings, $40 f(1 - \underline{S}_g) a(\underline{S}_w, 0)$. On the water-oil edge ($\underline{S}_g = 0$), the capillary pressure $p_g - p_o$ vanishes so that $p_g - p_w$ is contributed by $p_o - p_w$, namely $30 f(1 - \underline{S}_o) + 100 f(\underline{S}_w) \underline{S}_o$ which equals $(30 + 100 \underline{S}_o) f(\underline{S}_w)$. On the oil-gas edge ($\underline{S}_w = 0$), $p_g - p_w$ is contributed by $p_o - p_w$ which is unbounded, while $p_g - p_o$ remains bounded so that $p_g - p_w \simeq 100 f(\underline{S}_w) \underline{S}_o$.

It should be remarked that the above capillary pressure relations were not adopted from the literature but were newly built, based on the expected behavior along the sides of the saturation triangle considering a water-wet rock. Thus, changing the order of wettability (i.e. considering an oil-wet or mixed-wet material) would imply rebuilding completely the capillary pressure expressions. Moreover, as already indicated, hysteretic effects are not accounted for, i.e. no distinction is made between the drainage and the imbibition curves.

4.1 Alternative capillary pressure models

Few models of capillary pressures in a three fluid phase context have been published in the open literature. Bell et al. [1986] used the following simple prototype relations,

$$p_{cow} = a_w (1 - \underline{S}_w)^{b_w}, \quad p_{cgo} = a_g (\underline{S}_g)^{b_g}, \quad (4.5)$$

where $a_w=140$ kPa, $a_g=100$ kPa, $b_w=0.71$ and $b_g=0.51$. T Eqn. 4.5 implies bounded values of capillary pressures p_{cow} and p_{cgo} , whose contours are respectively parallel to the oil-gas and water-oil edges of the irreducible saturation triangle.

Helland and Skjæveland [2004] exposed a systematic method to build three-fluid phase capillary curves, calculating pressure as the sum of a function representing decreasing saturation and a function representing increasing saturation. However, the applicability of these relations is essentially limited to mixed wet rocks. This approach is also used in the models discussed in Skjæveland et al. [2000] and Dale [2008].

Hustad [2002] and Hustad and Browning [2010] developed a procedure to account for hysteresis effects in both the relative permeabilities and the capillary pressures, based on the experimental measurements on both water wet and oil wet sandpacks by Bradford and Leij [1996]. However, these experiments mainly involve porous media with fractional wettability, and the capillary pressures involved are rather low, of the order of a few kPa.

4.2 Pressure driven scheme for the three-phase model

In a two-phase context, the capillary pressure-saturation relation (4.1) can be inverted analytically. In contrast, inverting the system of equations (4.3) for the saturations in a three-phase context is less straightforward. In fact, since only two effective saturations and two capillary pressures out of three are independent, it suffices to consider any two of the three equations (4.3) to obtain any two increments of effective saturation $d\underline{S} = (d\underline{S}_w, d\underline{S}_o, d\underline{S}_g)$ in terms of the three incremental pressures $d\underline{p} = (dp_w, dp_o, dp_g)$.

The above procedure is adopted in a mixed finite element scheme employed in our numerical simulations, which uses the capillary pressures as the primary variables. In this context, the smoothness of the capillary pressure versus saturation curves is of considerable importance, as it directly influences the convergence rate of the iterative process that is required to ensure the conservation laws of the fluid masses (see Appendix B for details on the relevant algebraic aspects). A practical, numerical difficulty comes from the fact that, while the saturation domain is bounded, the capillary pressures may become infinite along (parts of) the edges of the saturation triangle. In this context, accounting for hysteresis would pose an additional numerical issue.

5 Simulation of gas injection into a deformable core

5.1 Initial, boundary conditions and numerical settings

The simulations hereby described aim at reproducing gas flooding of a deformable core of length $L = 0.3$ m. Its initial saturation with water and oil is uniform in space, as indicated in Fig. 5.1. The associated mass densities and volume fractions are reported in Table 5.1.

Table 5.1 Initial mass densities and volume fractions of fluids. The initial porosity (total volume fraction of the three fluids) is equal to 0.4.

	water	oil	gas
mass densities (kg/m ³)	$\rho_w = 1000$	$\rho_o = 1010$	$\rho_g = 1$
volume fractions	$n_w = 0.24$	$n_o = 0.16$	$n_g = 0.0$

Gas injection starting at time $t = 0^+$ s is simulated in 1D adopting the hydraulic boundary conditions shown in Fig. 5.3. At the outlet, corresponding to $x = 0$, the core is put in contact with a water reservoir. This process is numerically simulated by bringing, in a short time interval, the oil and gas pressures to the same value as water pressure (see fig. 5.3), thus quickly leading the outlet ($x = 0^+$) water saturation

$$\begin{array}{l}
\hline
S_w = 0.60; \quad p_{w0} = 100 \text{ kPa} \\
\hline
S_o = 0.40; \quad p_o = p_{w0} + p_{cow}(S_w, S_o, S_g) = 169 \text{ kPa} \\
\hline
S_g = 0; \quad p_g = p_{w0} + p_{cgw}(S_w, S_o, S_g) = 169 \text{ kPa} \\
\hline
\end{array}$$




Fig. 5.1 Initial conditions for a 1D gas injection test. The saturations are prescribed uniform over the core. The pressures and capillary pressures are deduced from the saturations based on the constitutive relations.

to reach $S_w = 1.0$. Meanwhile, the gas pressure is increased at the inlet, at $x = L$ (see fig. 5.3), thus maintaining the water and oil fluxes to zero from that end of the core. The fluid transport constitutive parameters are listed in Table 5.2.

As for the mechanical boundary conditions, the lateral displacement is set to vanish along the whole core, while the axial displacement at the inlet $x = L$ is set to zero. At the outlet $x = 0$, the total traction $\sigma_{xx}(x = 0, t)$ is kept fixed, and equal to the initial average fluid pressure $-\bar{p}(x = 0, t = 0) = -127.6 \text{ kPa}$, implying initially null applied effective stress. The sign convention adopted here considers as positive tensile stresses and extensive strains. The adopted bulk moduli values are provided in Table 5.3. Gas is considered ideal in its mechanical response. The solid grains are considered virtually incompressible (their bulk modulus being set to $K_s = 36 \text{ GPa}$), while the drained Poisson's ratio of the solid skeleton is set equal to 0.2.

The chosen finite element arrangement involves the use of four-node linear elements for the pressures, while a Q8 quadratic interpolation is adopted for the displacement. Two meshing configurations were adopted in the simulations, namely a fine mesh consisting of 63 elements and a coarse mesh of 18 elements. Both meshes are refined in the neighbourhood of the outlet, where the axial element size is progressively reduced up to one eighth of its value at core centre. A typical FEM mesh is represented in Fig. 5.2, with an indication of those nodal points where solid displacements are unknown and those where fluid pressures are unknown. The storage terms of the residuals and the tangent matrix are estimated at nodes, while the other terms are evaluated at $n_G \times n_G$ Gauss points, with $n_G = 2$. However, the number of Gauss points was found to affect the convergence rate. This point is discussed in more detail in Gajo et al. [2016], where also $n_G = 4$ has been considered.

Stable simulations require to set a minimum value k_r^{\min} for the relative permeabilities. In the simulations discussed below, values of $k_r^{\min} = 10^{-3}$ and intrinsic permeability $k_{in} = 1 \text{ darcy}$ are viewed as a reference, along with the finer mesh of 63 elements. To test the sensitivity of results to key parameter settings, additional simulations are run by altering the injection rate and some material parameters compared to the reference values. The capillary pressure relations (4.3) are adopted throughout. The irreducible saturations are all set to zero in this section (see Section 6 for non-zero irreducible saturation settings). While the Brooks-Corey model is adopted as the reference model for the relative permeabilities, further simulations are run to test the performance of the alternative models described in Sect. 3.3.

Table 5.2 Intrinsic permeability of a reservoir rock of good permeability (10^{-15} m^2 and 10^{-11} m^2 are considered poor and very good) and viscosities at ambient temperature, Maloney et al. [1989], Moulu et al. [1995], Muggerridge et al. [2014].

intrinsic permeability	viscosity		
	water	oil	gas
10^{-12} m^2	1 cP	2 cP	0.01 cP

Table 5.3 Bulk moduli.

bulk modulus (GPa)	solid skeleton	solid grains	water	oil
		0.555	36	2.2

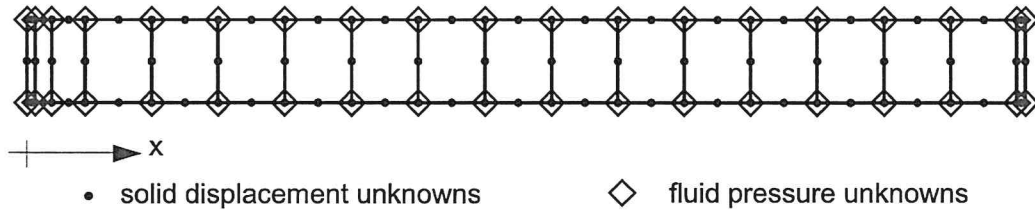


Fig. 5.2 Typical FEM coarse mesh, consisting of 18 elements. The mesh is refined especially in the neighbourhood of the outlet, where the axial element size is reduced by up to 1/8 of its value at core centre. Different symbols denote the integration points where solid displacement unknowns are evaluated, and those where fluid pressure unknowns are evaluated.

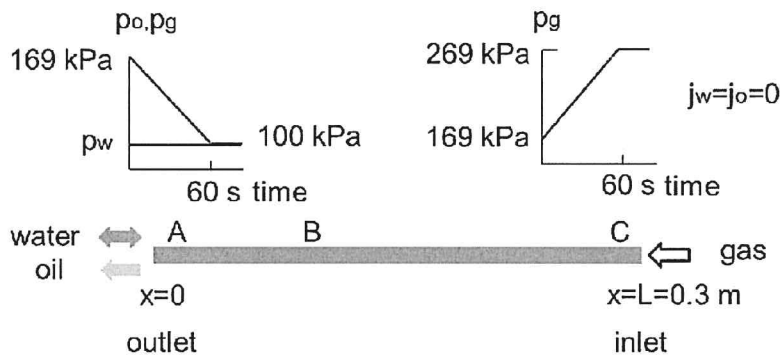


Fig. 5.3 Boundary conditions for a 1D core gas injection test. At the outlet, a) initially the pressure of the wetting fluid (water) is assumed equal to the pressure of the outlet reservoir; b) the oil and gas pressures are reduced to the water pressure in a short time interval at the end of which the specimen at $x = 0$ becomes water saturated. At the inlet, gas injection is pressure controlled and the water and oil fluxes, j_w and j_o respectively, vanish.

It should be finally observed that although simulations presented hereafter are one dimensional (a plane strain configuration with a single line of elements has been adopted), they are not restricted to this setting. In fact, the above outlined constitutive and computational formulations are two or three dimensional. However, by performing two or three dimensional simulations, unexpected issues that are not apparent in 1D computations might arise.

5.2 Three-phase results using the Brooks-Corey model

The simulations of gas injection are controlled by increasing the gas pressure at inlet over a short period of time. The propagation into the rock of this boundary signal through a gas saturation front that steepens as it reaches the outlet can be observed in Fig. 5.4-(a) and Fig. 5.4-(b). Subsequently, after gas breakthrough, the saturation profiles become smooth along the rock specimen. In fact, the saturation front becomes relatively modest in this phase and most of the changes of saturation take place progressively.

On the other hand, the pressure profiles of oil and water (Fig. 5.4-(c) and Fig. 5.4-(e)) establish rather quickly, and they are not far from their final levels at late times, when the boundary gas pressure attains its final value. Since the saturations are initially uniform, so are the initial relative permeabilities. In addition, since the pressures at the boundaries reach their final values quickly, the pressure profiles keep linear on the outlet side, until they are modified by the relative permeability changes emanating from the inlet.

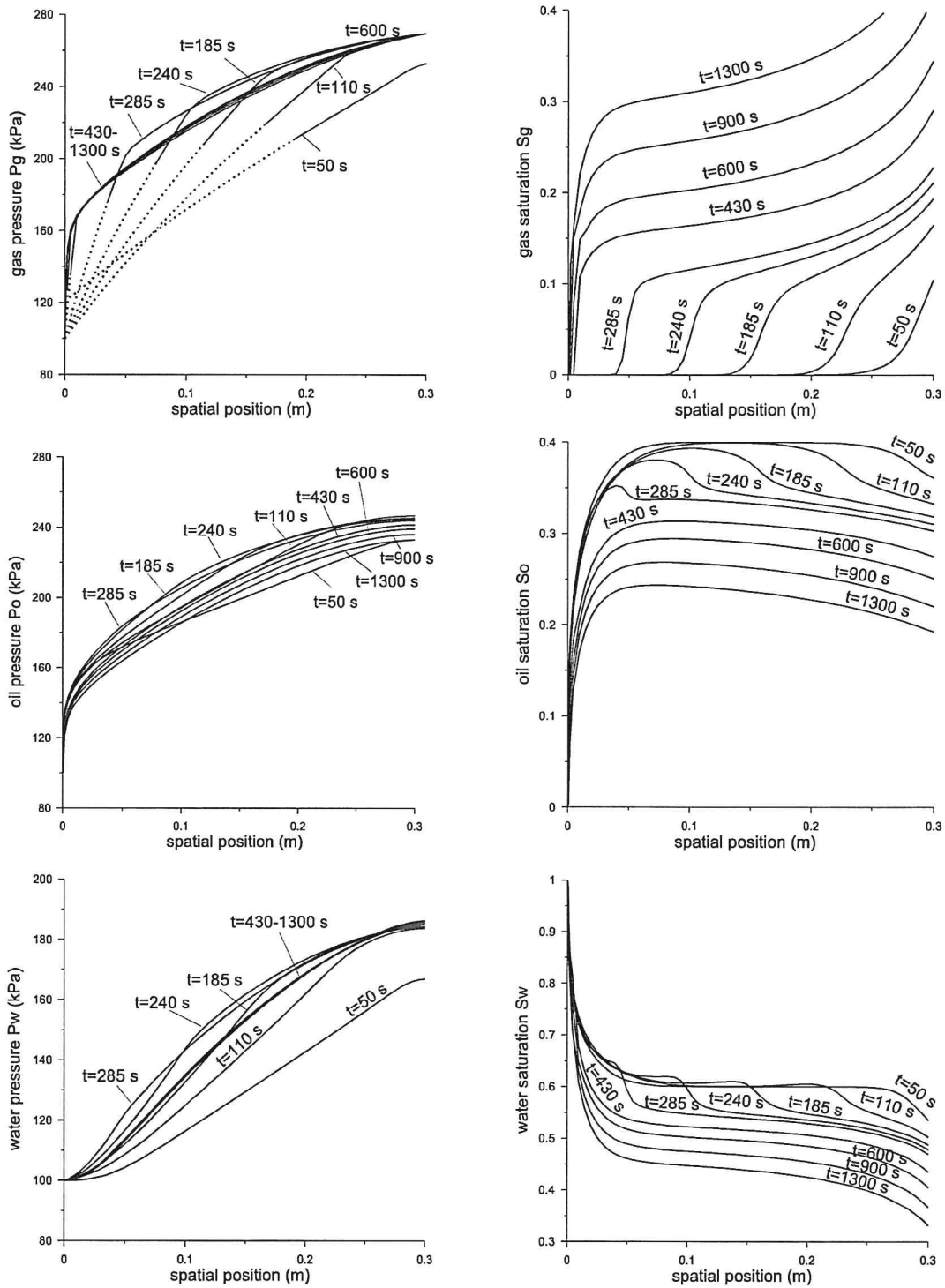


Fig. 5.4 Simulations of gas injection at $x = 0.3\text{m}$ using the Brooks-Corey model. Spatial profiles of water, oil and gas pressures and saturations at various times. The propagation of the fluids displays a front, which, although smooth, tends to steepen progressively over time until gas breakthrough. The dotted portions of the curves correspond to a vanishing gas saturation.

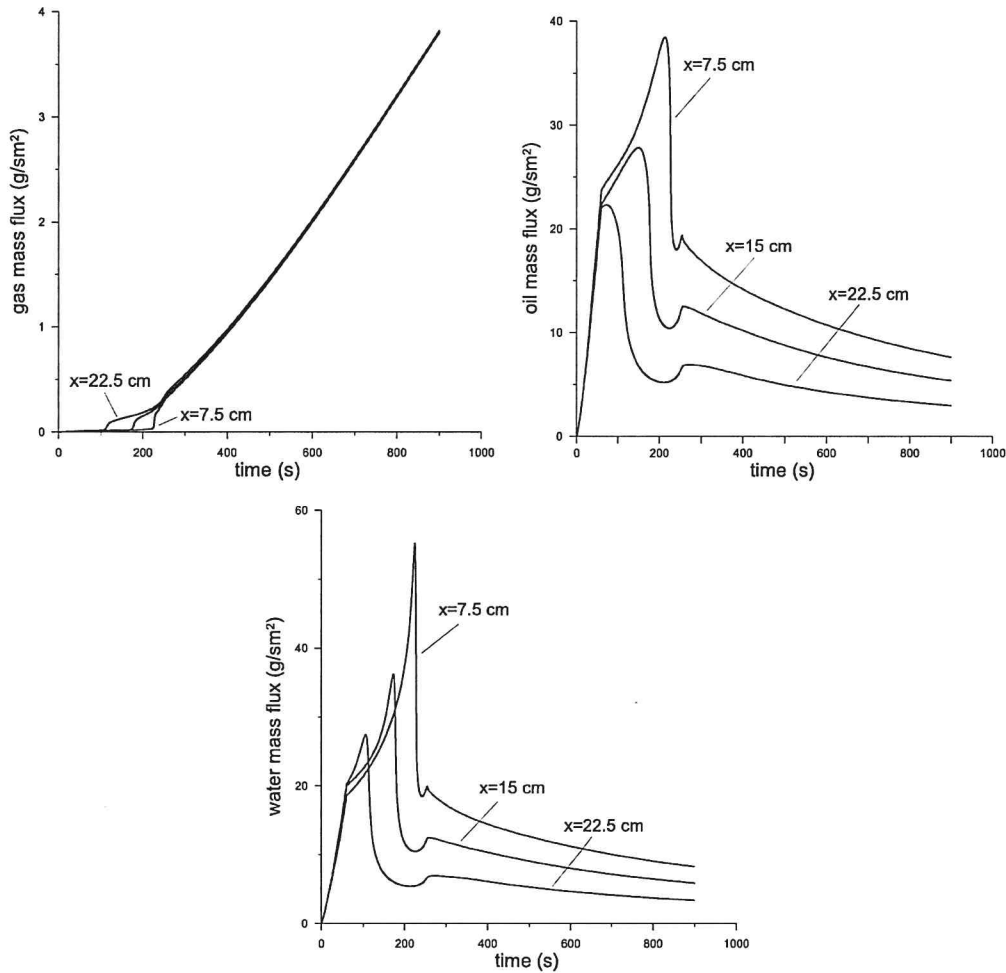


Fig. 5.5 Simulation of gas injection at $x = 0.3$ m using the Brooks-Corey model. Time evolution of the mass flux of (a) gas, (b) oil and (c) water during the injection process at three points along the core, located at 7.5, 15 and 22.5 cm from the outlet.

To explore the evolution of the three fluids' flow during gas injection, in Fig. 5.5 the mass fluxes of gas, oil and water are plotted vs time at three different core locations, corresponding to a region near the inlet ($x = 22.5$ cm), the core centre ($x = 15$ cm) and a region near the outlet ($x = 7.5$ cm). It can be observed that the gas flow, after breakthrough, is homogeneous along the core and increases monotonously with time. On the other hand the flows of oil and water are, expectedly, larger closer to the outlet, and exhibit two peaks, the first of which can be associated to the sudden contact with water, while the second is related to gas breakthrough.

The total traction applied at the outlet is kept to its initial value throughout the test. Consequently, the effective stress $\sigma'_{xx}(x = 0, t) = \bar{p}(x = 0, t) - \bar{p}(x = 0, t = 0)$, which is initially zero, becomes compressive (i.e., negative within our sign convention) as the specimen is put in contact with water and the oil and gas pressures are reduced. The strain is slightly contractive at this end while, along the core, Fig. 5.6-(a) shows that it becomes extensive at later times due to gas invasion.

The saturation path during the injection process, represented in the ternary diagram of Fig. 5.6-(b), highlights the two steps of pressure change at the boundaries, namely (i) the first contact with the water bath for 60s (along the water-oil edge, initial part of path A) followed by (ii) gas injection (second part of path A). The 900s gas injection results in oil production, its saturation decreasing from 0.4 to 0.1, and in a slightly smaller water production, its saturation decreasing from 0.6 to a position dependent value,

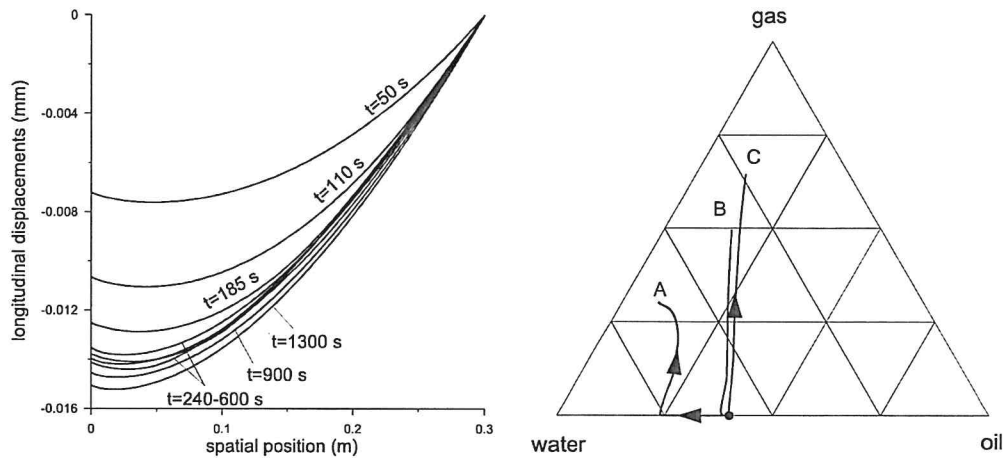


Fig. 5.6 Simulation of gas injection at $x = 0.3$ m using the Brooks-Corey model. (a) Spatial profiles of the displacement during the injection process; (b) Saturation paths at points A ($x=0.01$ m) close to outlet, B ($x=0.10$ m) at core center, and C ($x=0.29$ m) close to inlet, during gas injection for 900 s. The water inflow at early times, when the core is put in contact at the outlet with the water reservoir, is clearly apparent at point A.

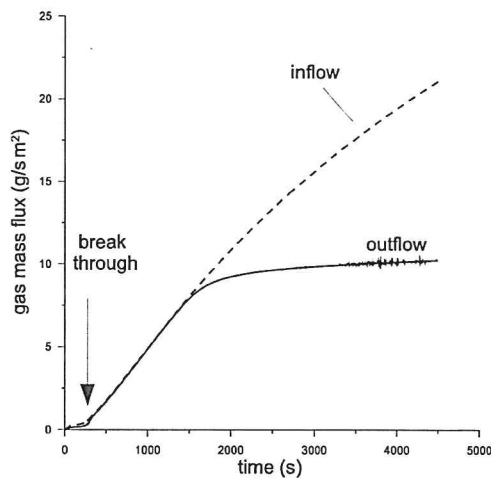


Fig. 5.7 Simulation of gas injection using the Brooks-Corey model. Time profiles of the mass flow of gas at inlet and outlet over a period of 5000 s.

namely 0.6 near the outlet and 0.25 near the inlet. The associated changes of relative permeabilities and capillary pressures along the path can be observed in Figs. 3.2 and 4.1 respectively.

The time profiles of gas mass flow at the inlet and outlet are shown in Fig. 5.7. Before gas breakthrough, occurring in this case after about 300 s, gas inflow at the inlet is slightly larger than outflow at the outlet. Gas breakthrough can also be detected from the propagation fronts of the saturations in Fig. 5.4 and from the peaks displayed by the oil mass outflow plot of Fig. 5.9. Another indication of gas breakthrough is displayed in Fig. 5.7, when the inlet and outlet gas mass fluxes tend to temporarily become equal. However, the subsequent profiles of the mass inflow and outflow of gas differ, because part of the injected gas remains in the core and increases its saturation. As the gas pressures are fixed at the inlet and outlet, the gas flux would be constant if the gas relative permeability was fixed. However, as the gas enters the core, its relative permeability increases. This permeability increase continues until gas saturates completely the core, at which point the gas inflow and outflow will both balance exactly and be constant. Fig. 5.7 indicates that the time required to reach steady state is much larger than 5000 s.

The sensitivity of the results to intrinsic/absolute permeability was explored, although it is not shown for the sake of brevity. It was found that a larger absolute permeability speeds up the propagation of the saturation front. The oil mass outflow at outlet showed two maxima, the first of which is due to the fact that the sample is suddenly put in contact with the water reservoir, while the second peak is related to gas breakthrough.

The influence of initial oil saturation was also explored. For a larger initial oil saturation ($S_w = 0.4$, $S_o = 0.6$, $S_g = 0$), the initial oil and gas pressures were found equal to 212 kPa, instead of 169 kPa for the reference initial saturation ($S_w = 0.6$, $S_o = 0.4$, $S_g = 0$). Consistently, in the larger initial oil saturation case, the gas pressure at inlet is raised to 300 kPa in 60 s so that the pressure differential between inlet and outlet is equal in both cases to 200 kPa. From the relative permeability contours of Fig. 3.2, it can be inferred that, if the saturation path lies closer to the water (bottom-left) vertex of the ternary diagram, the relative permeability to water is larger. The same remark holds for the oil relative permeability, if the path lies closer to the oil (bottom-right) vertex. Being the gas isoperms virtually horizontal (Fig. 3.2-(c)), no large effects on the gas permeability should be induced due to the modification of the initial oil saturation. Therefore the time profiles of gas saturation are expected to be similar for the two different initial oil saturation cases.

The injection rate can be controlled by decreasing the duration of the gas pressure increase at the inlet. Increasing the injection rate is expected to speed up the propagation of the saturation front and to increase the early outflow of oil. To check the model sensitivity to the rate of injection, the gas pressure at inlet was increased from 169 kPa to 269 kPa and to 300 kPa, corresponding to a differential pressure between inlet and outlet equal to 169 kPa and 200 kPa respectively. It emerged that at larger differential pressure, and correspondingly at larger injection rate, the propagation of the gas front is significantly faster (not shown here, for the sake of brevity).

5.3 Three-phase simulation results using alternative permeability models

While using the reference parameters of Sect. 5.1, the simulations of this section adopt alternative models of relative permeability to the Brooks-Corey relations (eqn 3.3), namely the Juanes-Patzek model, eqn (3.9), the Stone model, eqn (3.8), the symmetric formulation, eqn (3.6) and the bundle model eqn (3.10). The spatial profiles of the gas saturation along the core during the injection process are displayed in Fig. 5.8. Similar to the Brooks-Corey model, gas injection induces a saturation propagation front for the model of Juanes-Patzek (a) and the symmetric formulation with $\omega = 2$ (d). On the other hand, the front propagation is not apparent for the model of Stone (b), the symmetric formulation with $\omega = 1$ (c) and the bundle model (f), as these models result in a very fast, although finite, propagation of the gas saturation, followed by a diffusion-like behaviour. As anticipated in Sect. 3.4, this feature is not linked to a loss of hyperbolicity, since, for example, the symmetric formulation with $\omega = 1$ remains strictly hyperbolic within the saturation triangle, even if some of the apices of the saturation triangles might be umbilic points. Moreover, regardless of whether the speed of propagation of the saturation front is large or not, the characteristic rates of increase of saturation after gas breakthrough are very similar for all models.

The time profile of the oil mass outfluxes is reported for all models in Fig. 5.9. These mass fluxes reflect the mode of propagation of the gas. Similar to the Brooks-Corey model, the first maximum of the flux is associated with the sudden contact with water for all models. The second maximum is related to the gas breakthrough for the models that show a slow propagation front, namely the Brooks-Corey model, the Juanes-Patzek model and the symmetric formulation with $\omega = 2$. On the other hand, the breakthrough is not visible for the models that display a fast propagation front: the two peaks are simultaneous, i.e. breakthrough occurs at the same time as the oil outflow due to the contact with the reservoir. For the Stone model, oil accumulates progressively close to the outlet during the injection process, its exit is delayed and starts being effective at about 900 s only.

A mesh sensitivity analysis, that is not shown for the sake of brevity, has been performed. For the Brooks-Corey model, the Juanes-Patzek model and the symmetric formulation with $\omega = 2$, the coarser mesh induces some oscillations in the propagation front that, however, fade out with time. In contrast, both the fine and coarse meshes yield very similar saturation curves for those models displaying a diffusion-like behaviour after gas breakthrough, namely for the Stone model and the symmetric formulation with $\omega = 1$.

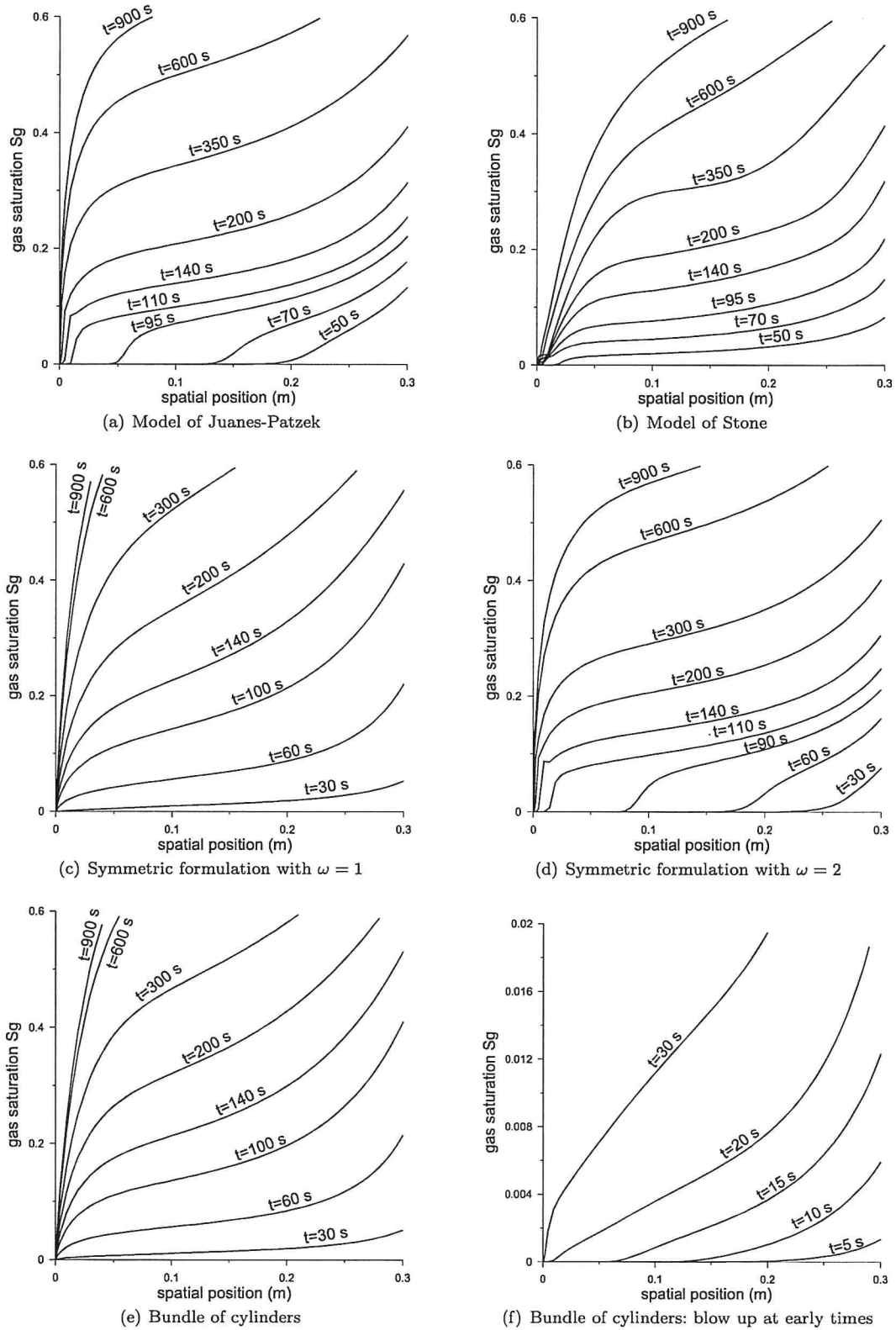


Fig. 5.8 Simulations of gas injection at $x = 0.3\text{m}$ using the models of (a) Juanes-Patzek, (b) Stone, (c) symmetric formulation with $\omega = 1$ and (d) $\omega = 2$, (e) bundle model and (f) blow up of the response of the latter model at early times. Space profiles of gas saturation during the process. The propagation of the gas front is much faster for the models of Stone, the symmetric formulation with $\omega = 1$ and the bundle model.

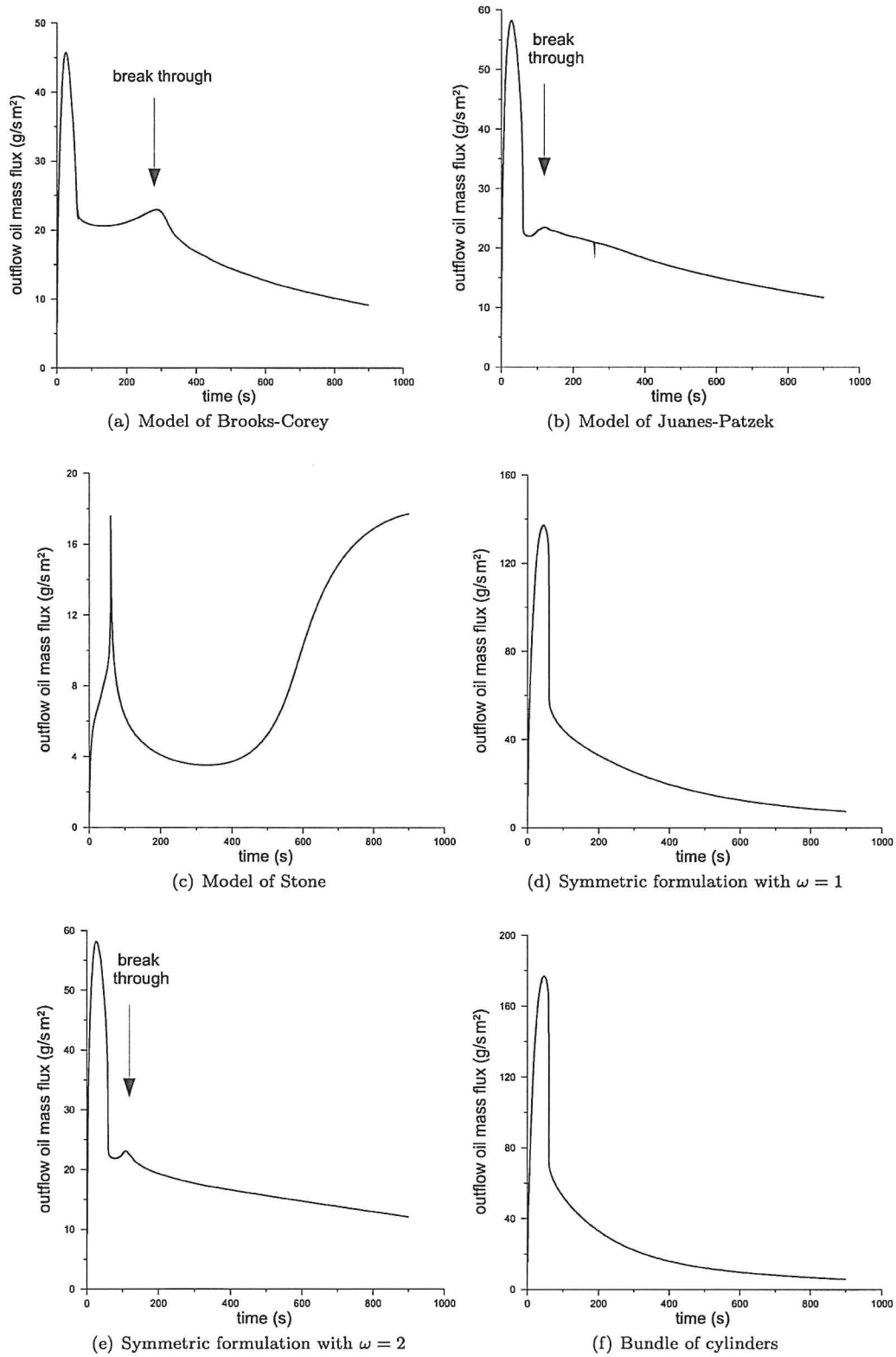


Fig. 5.9 Simulations of gas injection at $x = 0.3\text{m}$ using the models of (a) Brooks-Corey, (b) Juanes-Patzek, (c) Stone, symmetric formulation with (d) $\omega = 1$ and (e) $\omega = 2$, and (f) bundle model. Time profiles of oil mass flux at outlet during the process.

5.4 Simulations of water-alternating-gas injection with the Brooks-Corey model

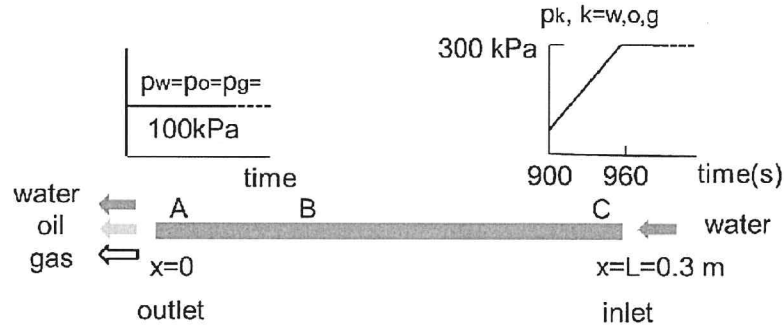


Fig. 5.10 Boundary conditions for water injection subsequent to gas injection during 900s. At the outlet, the pressures are kept to their current values. At the inlet, the pressures are increased to a common value in 60s.

The Brooks-Corey permeability model has also been used to simulate water-alternating-gas (WAG) injection experiments. Upon gas injection, most experiments described in the literature show first oil production, followed by water production. However, this trend is not expected if the oil saturation (at injection) is close to the irreducible oil saturation. In such cases, gas injection brings about water production. In fact, more generally, the saturation paths are limited by the tangents to the irreducible saturation triangle. As an example, in the WAG coreflooding experiments of Shahverdi [2012] on two rocks of rather different permeabilities (0.065 and 1 darcy), water is produced initially, followed by oil production. Controlling the pressure differential instead of the injection rate, Moulu et al. [1995] presented similar experimental saturation paths.

Gas injection was simulated with the same settings as in Sect. 5.2, but it was then discontinued at 900s and replaced by water injection. The boundary conditions for the second part of the experiment involving water injection are schematized in Fig. 5.10. The space profiles of pressures and saturations during the process are displayed in Fig. 5.11. Water injection results in a larger dilatation of the core than gas injection, Fig. 5.12-(a). Water injection sweeps gas, but it is not efficient enough in completely expelling oil, as can be seen in the saturation paths of Fig. 5.12-(b) and time profile of oil outflux in Fig. 5.13. For a correct interpretation of these simulations, it should be recalled that neither the relative permeabilities nor the capillary pressures include hysteresis effects.

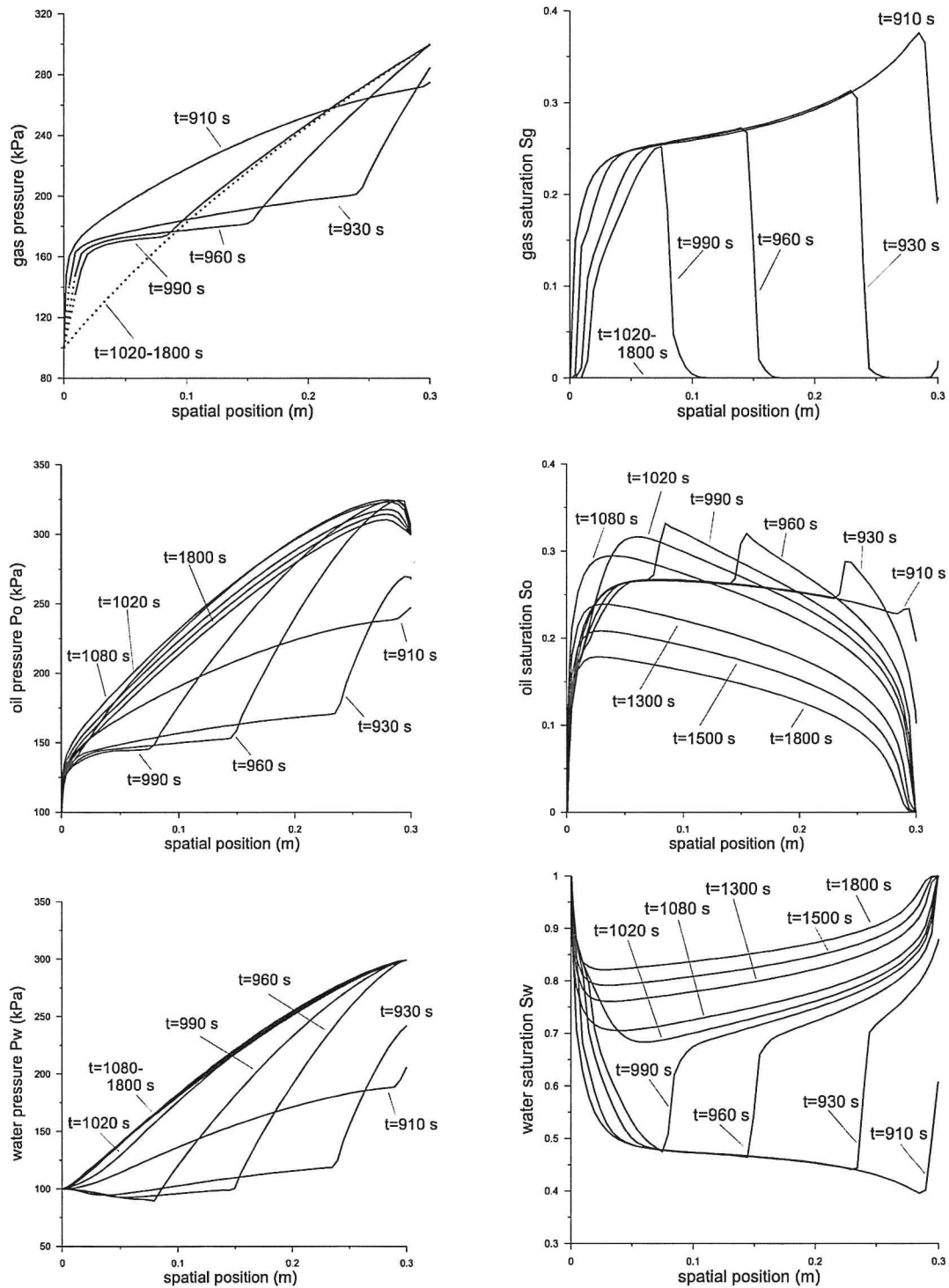


Fig. 5.11 Simulation of gas injection at inlet ($x = 0.3$) m up to 900 s followed by water injection using the Brooks-Corey model. Spatial profiles of pressures and saturations for water, oil and gas at various times. Water injection is obtained by increasing to 300 kPa all pressures at inlet in 60 s. The dotted portions of the curves correspond to a vanishing gas saturation.

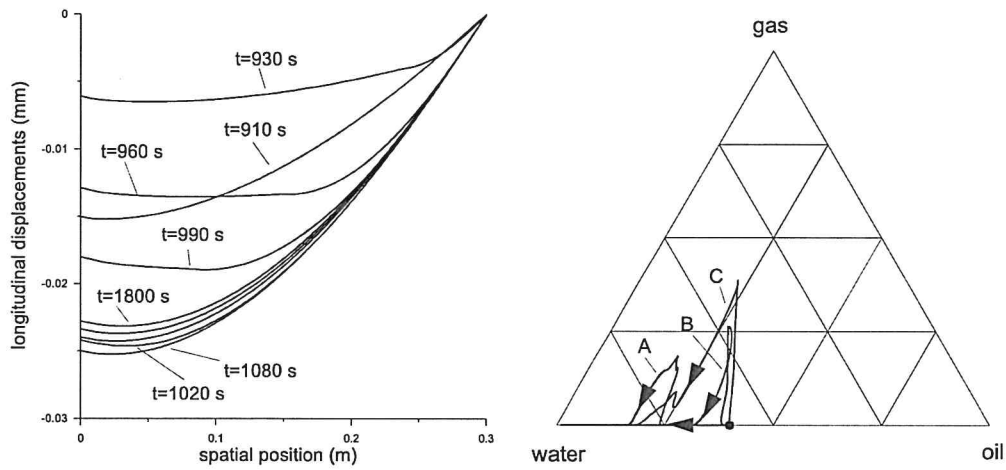


Fig. 5.12 Simulation of gas injection up to 900 s followed by water injection (at $x = 0.3$ m) using the Brooks-Corey model. (a) Spatial profiles of the displacement during the injection process; (b) saturation paths at points A ($x=0.01$ m) close to outlet, B ($x=0.10$ m) at core center, and C ($x=0.29$ m) close to inlet, during gas injection for 900 s followed by water injection, leading to a sharp U-turn towards the water apex.

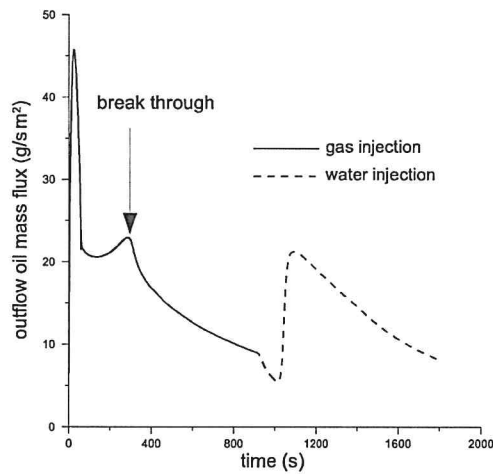


Fig. 5.13 Simulation of gas injection for 900 s followed by water injection using the Brooks-Corey model. Time profiles of the mass outflow of oil at outlet.

Table 6.1 Irreducible saturations, after Hustad [2000].

water-oil	$S_{wro} = 0.15$	$S_{orw} = 0.2$
oil-gas	$S_{org} = 0.04$	$S_{gro} = 0.03$
gas-water	$S_{grw} = 0.06$	$S_{wrg} = 0.05$

Fig. 6.3. Water imbibition results in a steep propagation front for the gas saturation. The water and oil saturations display propagation fronts too, but of lesser amplitude. Indeed, the so-called mobility ratio of the displacing fluid ($a = w$) versus displaced fluids ($p = o, g$),

$$M = \frac{k_{ra}}{k_{rp}} \frac{\eta_p}{\eta_a}, \quad (6.1)$$

is equal to 2 for the water-oil system and to 0.01 for the water-gas system. This ratio is known to be an indicator of the ease of the sweep: more efficient displacement is obtained for mobility ratios lower than one. In fact, gas is expelled in a relatively short time out of the specimen.

The time for the gas front to reach the right end is about 300 s, and, by 750 s, its saturation at this end has been reduced by more than half (Fig. 6.3-(b)). These figures are in line with the characteristic time for strongly water-wet systems in the absence of gravity effects, expressed by Ma et al. [1997] as

$$\tau_D = L^2 \frac{\sqrt{\eta_w \eta_o}}{\sigma_{wo} \cos \theta_{wo}} \sqrt{\frac{n}{k_{in}}}, \quad (6.2)$$

where $k_{in} = 10^{-12} \text{ m}^2$ the intrinsic permeability, $n = 0.4$ porosity, $\sigma_{wo} = 50 \text{ mN/m}$ the water-oil interfacial tension (IFT), $\theta_{wo} = 0^\circ$ for a strongly water wet rock, $\eta_w = 10^{-3} \text{ Pa}\cdot\text{s}$ and $\eta_o = 2 \times 10^{-3} \text{ Pa}\cdot\text{s}$ the viscosities, $L = 0.3 \text{ m}$ the core length for co-current imbibition (twice that length must be considered for counter-current imbibition). The resulting characteristic times τ_D are equal to 1600 s and 6400 s respectively for co-current and counter-current imbibition. On the other hand, for two-phase water-gas saturation with $\sigma_{wg} = 50 \text{ mN/m}$ water-gas IFT and $\eta_g = 2 \times 10^{-5} \text{ Pa}\cdot\text{s}$, the characteristic time τ_D is equal to about 110 s and 440 s respectively for co-current and counter-current imbibition.

Since gas is expelled quickly, the saturation path is initially directed towards the water-oil side of the saturation triangle (at later times, it will tend towards the water apex), as can be seen in Fig. 6.4-(b). Along the path, the capillary pressure $p_g - p_w$ displays a maximum, as can be also deduced comparing Fig. 6.4-(b) and Fig. 4.1-(c). This maximum is larger for saturation paths closer to the oil apex. Hence, the capillary pressure $p_g - p_w$ temporarily reaches a large value, resulting in a temporary burst of the gas pressure and increase of the water pressure in the vicinity of the right end of the core (for which the saturation path comes closer to the oil apex). At the same time, oil is pushed to the core's right end and it gets somehow trapped there. Once the water front reaches the right end of the core, its saturation increases at the expense of oil, since the system at this point is virtually two-phase. Thus, oil starts flowing back towards the core left end. This process begins at about 1250 s. Estimating the characteristic time using eqn (6.2), oil saturation is not expected to significantly decrease before about 5000 s.

The total traction applied at the left end is maintained to its initial value. The effective stress $\sigma'_{xx}(x = 0, t) = \bar{p}(x = 0, t) - \bar{p}(x = 0, t = 0)$, which is initially zero, becomes tensile when the saturations of oil and gas are reduced to their irreducible values as the average pressure increases all along the core (Fig. 6.3). As a consequence the core undergoes extension, and displacement takes place toward the free end, see Fig. 6.4-(a). The simulated saturation paths along the core corroborate the above description, in that gas is expelled first, and water flooding begins first closest to the inlet, at $x = 0$. The extensive strain seems uniform along the whole core after as early as 1000 s upon imbibition (Fig. 6.4-(a)), although at this time the pressures and saturations of water and oil are still very much heterogeneous.

The pressure and saturation profiles shown in Fig. 6.3 were obtained with both coarse (dashed lines) and fine (solid lines) mesh, as described in Sect. 6.1. Clearly, the mesh sensitivity is not significant.

7 Conclusion and outlook

A comprehensive framework was developed to reproduce some key features of the coupled hydro-mechanical behaviour of porous media saturated by three immiscible fluids, with a number of applications in environ-

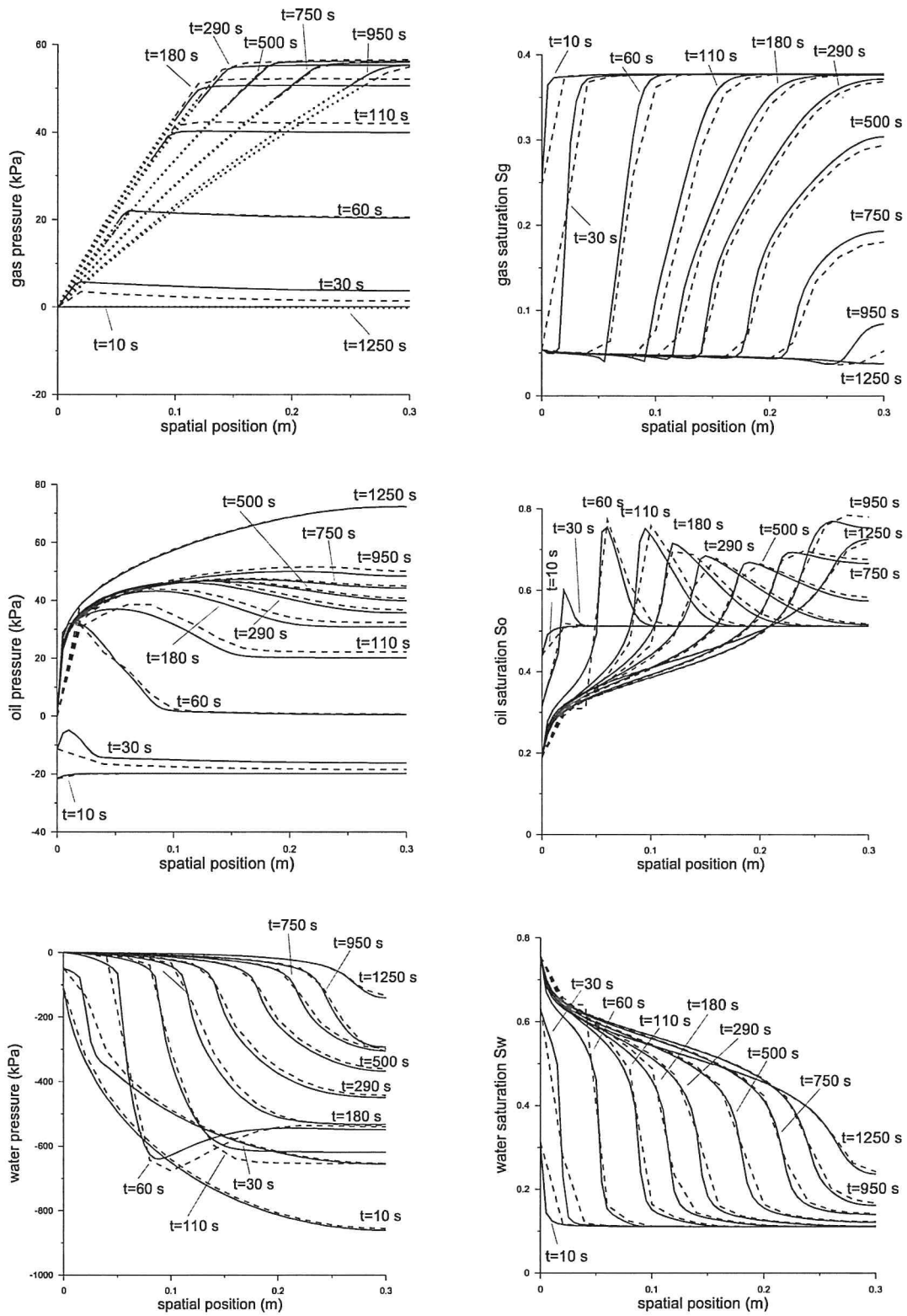


Fig. 6.3 Simulation of a counter-current imbibition test at $x = 0$ using the Brooks-Corey model, the coarse mesh (dashed curve) and fine mesh (solid curve) and minimum relative permeability ($k_r^{\min} = 10^{-3}$). Spatial profiles of water, oil and gas pressures and saturations are shown at various times. The dotted portions of the curves correspond to a vanishing gas saturation.

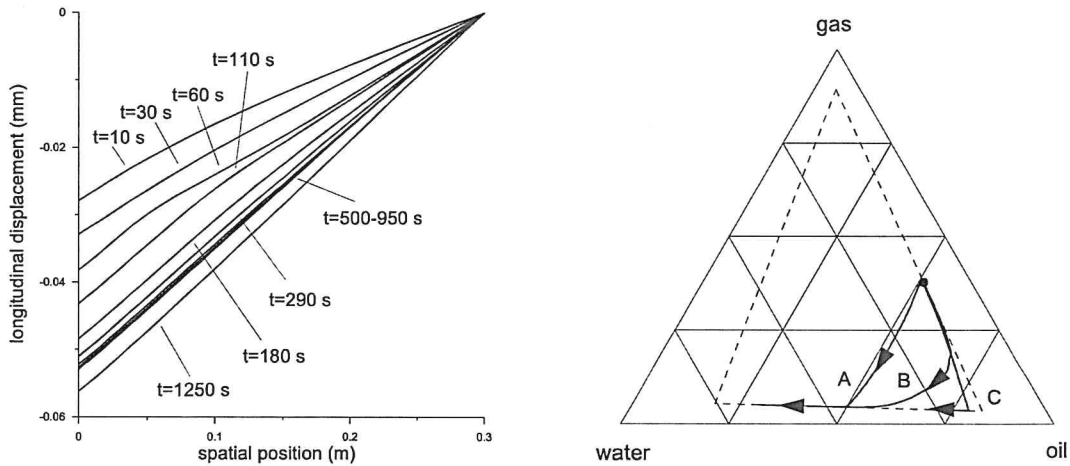


Fig. 6.4 Simulation of a counter-current imbibition test at $x = 0$ using the Brooks-Corey model, the coarse mesh and minimum relative permeability ($k_r^{\min} = 10^{-3}$). (a) Spatial profiles of displacement during the tests; (b) saturation paths at points A ($x=0.02$ m) close to water inlet, B ($x=0.16$ m) at core center, and C ($x=0.28$ m) close to right end, during the counter-current imbibition test for 1250 s. The water inflow at early times, when the core is put in contact with the water reservoir at the left end is clearly apparent at point A. At variance, at points B and C, gas is first expelled through the left end and replaced by oil.

mental and energy engineering. Different constitutive equations for the relative permeabilities and capillary pressures have been tested under different loading conditions aiming at reproducing realistic applications, especially relevant to the flow of gas, oil and water in a deformable rock. Petroleum engineering applications in particular are considered, due to a relative abundance of experimental data, however this framework can be readily applied to other problems involving the co-existence of three immiscible fluids, such as groundwater pollution and CO₂ sequestration problems. The finite element simulations include the standard 1D core flooding laboratory tests on water wet rock samples, namely gas injection into a core initially saturated by oil and water, water-alternated-gas injection into a core initially saturated by oil and water, and counter-current imbibition tests into a core initially saturated by oil, water and gas. The effects on the simulations of the different constitutive assumptions for the relative permeabilities are examined in detail.

Emphasis has been laid here on the constitutive equations governing the relative permeabilities and capillary pressures for water-wet rocks saturated by water, oil and gas. Few constitutive models defining the relative permeabilities in a three fluid phase context have been published. Most of them are actually rather prototypes than complete models. The state of affairs is quite similar as far as constitutive models of capillary pressures are concerned. While the present developments do not claim to match the fine details of the flow response of specific rock samples, the proposed constitutive framework is simple and complete. Implementation in an existing domestic finite element code, initially devoted to water saturated rocks, demonstrates the versatility and modularity of this approach. Moreover, the successful simulations of the main experimental tests that are reported in the literature, namely gas injection, water alternating gas injection and counter-current imbibition, are considered as an additional test of the robustness of the framework.

The tests have considered jacketed cores and therefore reduced the solid displacement vector and fluid fluxes to their sole axial components. However, the constitutive framework is essentially three-dimensional, and, in fact, the simulations have been performed in an axisymmetric context, with the radial displacement prevented.

The strong nonlinearities associated with the relative permeabilities lead to severe pressure gradients that need to be addressed by special techniques. The computational aspects of the finite element implementation and the details of the time marching scheme are deferred to another publication, Gajo et al. [2016].

Extending the model to include thermal effects and phase change constitutes the next challenge. As a preliminary step, the constitutive equations implemented in this work for the mechanical response of water and gas follow the general framework developed in IAPWS [2002] which is tailored to a non isother-

mal context, prone to phase change (vaporization, condensation), including the temperature and pressure dependence of the viscosities. Further analysis will also require the development of thermomechanical constitutive equations for oil. In this perspective, the elastic linear mechanical response need to be upgraded to an elastic-plastic response to account for dilatation effects that are of prime importance in increasing the absolute permeabilities on the sides of the steam chamber during steam assisted gravity drainage of oil recovery processes.

The constitutive expressions of the three-phase capillary pressures that have been proposed are restricted to water-wet rocks. Extension of this framework to mixed-wet rocks represents another challenge.

Acknowledgements

A. Gajo and F. Cecinato acknowledge support from the EU research project ERC-2013-ADG-340561-INSTABILITIES. B. Loret acknowledges support from the "Visiting Professor 2013" program of the University of Trento.

References

1. Abdallah W., Buckley J.S., Carnegie A., Edwards J., Herold B., Fordham E., Graue A., Habashy T., Seleznev N., Signer C., Hussain H., Montaron B. and Ziauddin M. (2007). Fundamentals of Wettability. *Oilfield review*, 19(2), 44-61.
2. Alizadeh A.H. and Piri M. (2013). Effect of saturation history on three-phase relative permeability: an experimental study. International Symposium of the Society of Core Analysts, Napa Valley, 16-19 September 2013, Paper Number SCA2013-23, 12 pp.
3. Amiri, S. G., Sadrnejad, S. A., Ghasemzadeh, H., Montazeri, G. H. (2013). Application of control volume based finite element method for solving the black-oil fluid equations. *Petroleum Science*, 10(3), 361-372.
4. Anderson W.G. (1987). Wettability literature survey. Part 5: The effects of wettability on relative permeability. *J. Petroleum Technology*, Nov. 1987, 1453-1468.
5. Behbahani H. and Blunt M.J. (2005). Analysis of imbibition in mixed-wet rocks using pore-scale modeling. *Society of Petroleum Engineers J.*, 466-473.
6. Bell J.B., Trangenstein J.A. and Shubin G.R. (1986). Conservation Laws of Mixed Type Describing Three-Phase Flow in Porous Media. *SIAM Journal on Applied Mathematics*, 46(6), 1000-1017. URL: <http://www.jstor.org/stable/2101655>
7. Binning P., Celia M. A. (1999). Practical implementation of the fractional flow approach to multi-phase flow simulation. *Advances in Water Resources*, 22(5), 461-478.
8. Bradford S.A. and Leij F.J. (1996). Predicting two- and three-fluid capillary pressure-saturation relationships of porous media with fractional wettability. *Water Resources Research*, 32(2), 251-259.
9. Brooks R.H. and Corey A.T. (1964). Hydraulic Properties of Porous Media. Colorado State University, Hydro paper No.5.
10. Corey A.T., Rathjens C.H., Henderson J.H. and Wyllic M.R.J. (1956). Three-phase relative permability, Transactions of The American Institute of Mining, Metallurgical, and Petroleum Engineers (AIME), 207, 349-351, or *J. Petroleum Technology*, 8(11), 63-65.
11. Chalaturnyk R.J. (1996). Geomechanics of the Steam Assisted Gravity Drainage. PhD thesis, University of Alberta, Edmonton, Canada.
12. Chen, Z. (2000). Formulations and numerical methods of the black oil model in porous media. *SIAM Journal on Numerical Analysis*, 38(2), 489-514.
13. Dale E.I. (2008). Modelling of immiscible WAG with emphasis on the effect of capillary pressure. PhD thesis, University of Bergen, Norway.
14. Delshad M. and Pope G.A. (1989). Comparison of the Three-Phase Oil Relative Permeability Models. *Transport in Porous Media*, 4, 59-83.
15. El-Amin M.F. and Sun S. (2011). Effects of gravity and inlet/outlet location on two-phase cocurrent imbibition in porous media. *J. Applied Mathematics*, Article ID673523, 18 p, doi:10.1155/2011/673523.
16. Egermann P., Mejdoub K., Lombard J.-M., Vizika O. and Kalam Z. (2013). Drainage three-phase flow relative permeability on oil-wet carbonate reservoir rock-types: experiments, interpretation and comparison with standard correlations. International Symposium of the Society of Core Analysts, Napa Valley, 16-19 September 2013, Paper Number SCA2013-A028, 14 pp.
17. Forsyth, P. A., Shao, B. Y. (1991). Numerical simulation of gas venting for NAPL site remediation. *Advances in Water Resources*, 14(6), 354-367.
18. Gajo A., Cecinato F. and Loret B. (2016). Finite element simulations of flooding in a deformable core saturated by three immiscible fluids. Submitted to *International Journal for Numerical Methods in Engineering*.
19. Grivot P., Bouvier L., Fournier J. and Silverii A. (1995). Residual oil saturation and multiphase relative permeability measurements on a water-wet sandstone reservoir and a limestone reservoir of mixed wettability. International Symposium of the Society of Core Analysts, San Francisco, 12-14 September 1995, Paper 9503, 10 pp.
20. Helland J.O. and Skjæveland S.M. (2004). Three-Phase Capillary Pressure Correlation For Mixed-Wet Reservoirs. International Petroleum Conference in Mexico held in Puebla, Mexico, 8-9 November 2004, paper SPE 92057.

21. Huang D.D., Honarpour M.M. and Al-Hussainy R. (1997). An improved model for relative permeability and capillary pressure incorporating wettability. 1997 SCA International Symposium Calgary, Canada, September 7-10, 1997, paper SCA-9718.
22. Hustad O.S. (2000). Simulation examples using a fully coupled model for three-phase capillary pressure and relative permeability with hysteresis. Sintef Petroleum Research, Trondheim, Norway, March 2000.
23. Hustad O.S. (2002). A Coupled Model for Three-Phase Capillary Pressure and Relative Permeability, Society of Petroleum Engineers J., 7(1), 59-69.
24. Hustad O.S. and Browning D.J. (2010). A fully coupled three-phase model for capillary pressure and relative permeability for implicit compositional reservoir simulation. Society of Petroleum Engineers J., Paper 125429, 1009-1025.
25. IAPWS (2002). The IAPWS Formulation 1995 for the Thermodynamic Properties of Ordinary Water Substance for General and Scientific Use. Wagner W. and Pruss A. eds., J. Physical Chemical Reference Data, 31, 387-535.
26. Juanes R. and Patzek T. (2004). Relative Permeabilities for Strictly hyperbolic Models of Three-Phase Flow in Porous Media. Transport in Porous Media, 57, 125-152.
27. Jackson M.D. and Blunt M. (2002). Elliptic Regions and Stable Solutions for Three-Phase Flow in Porous Media Transport in Porous Media, 48, 249-269.
28. Leverett, M., Lewis, W. B. (1941). Steady flow of gas-oil-water mixtures through unconsolidated sands. *Transactions of the AIME*, 142(01), 107-116.
29. Li K. (2004). Theoretical Development of the Brooks-Corey Capillary Pressure Model from Fractal Modeling of Porous Media. 2004 SPE/DOE Fourteenth Symposium on Improved Oil Recovery held in Tulsa, Oklahoma, U.S.A., 17-21 April 2004.
30. Ma S., Morrow N.R. and Zhang X. (1997). Generalized scaling of spontaneous imbibition data for strongly water-wet systems. J. Petroleum Engineering and Science, 18, 165.
31. Maloney D., Mahmood S.M. and Honarpour M.M. (1989). The effects of viscous forces on three-phase relative permeability. Report for the US Department of Energy, NIPER-392 (DE89000737).
32. Morel-Seytoux J. (1973) Two-phase flow in porous media. In: *Advances in hydroscience*, Vol. 9, V.T. Chow, ed. New York: Academic press, 120-202.
33. Moulou J.C., Kalaydjian F. and Martin J.-M. (1995). Performance and numerical interpretation of gas drainage core tests under secondary and tertiary conditions. International Symposium of the Society of Core Analysts, San Francisco, 12-14 September 1995, Paper 9508, 11 pp.
34. Mroginski, J. L., Di Rado, H. A., Beneyto, P. A., Awruch, A. M. (2010). A finite element approach for multiphase fluid flow in porous media. *Mathematics and Computers in Simulation*, 81(1), 76-91.
35. Muggeridge A., Cockin A., Webb K., Frampton H., Collins I., Moulds T. and Salino P. (2014). Recovery rates, enhanced oil recovery and technological limits. *Philosophical Transactions Royal Society A* 372: 20120320. <http://dx.doi.org/10.1098/rsta.2012.0320>
36. Pao, W. K., Lewis, R. W., Masters, I. (2001). A fully coupled hydro-thermo-poro-mechanical model for black oil reservoir simulation. *International journal for numerical and analytical methods in geomechanics*, 25(12), 1229-1256.
37. Shahverdi H. (2012). Characterization of Three-phase Flow and WAG Injection in Oil Reservoirs. PhD thesis, Heriot-Watt University, Edinburgh, UK.
38. Shahverdi H., Sohrabi M., Fatemi M. and Jamiolahmady M. (2011). Three-phase relative permeability and hysteresis effect during WAG process in mixed wet and low IFT systems. J. Petroleum Science and Engineering, 78, 732-739.
39. Skjæveland S.M., Siqveland L.M., Kjosavik A., Hammervold Thomas W.L. and Virnovsky G.A. (2000). Capillary Pressure Correlation for Mixed-Wet Reservoirs. SPE Reservoir Evaluation & Engineering 3, 60-67.
40. Standing M.B. (1975). Notes on relative permeability relationships. Unpublished notes, revised in 1978. University of Trondheim, Norway.
41. Suicmez V.S., Piri M. and Blunt M.J. (2006). Pore scale modeling of three-phase WAG injection: prediction of relative permeabilities and trapping for different displacement cycles. SPE/DOE Symposium on Improved Oil Recovery, Tulsa, Oklahoma, USA, 22-26 April 2006, SPE 95594, pp. 14.
42. van Genuchten, M.T. (1980). A closed-form equation for predicting the hydraulic conductivity of unsaturated soils. *Soil Science Society America J.* 44, 892-898.
43. Weifeng L., Zubo Z., Qingjie L., Desheng M. and Kangyun W. (2012). Measurement of three-phase relative permeabilities of various saturating histories and wettability conditions. International Symposium of the Society of Core Analysts, Aberdeen, Scotland, 27-30 August 2012, SCA2012-43, 6 pp.
44. Yin S., Dusseault M.B., Rothenburg L. (2009) Thermal reservoir modeling in petroleum geomechanics. *International journal for numerical and analytical methods in geomechanics* ; 33(4): 449-85.

Appendix A: Useful relations for the three-phase effective saturations

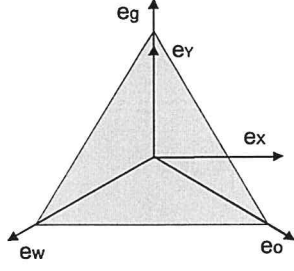


Fig. A.1 Axes (e_x, e_y) in the plane of the triangle \mathcal{T} .

With reference to Fig. A.1, the saturations,

$$\mathbf{S} = S_w \mathbf{e}_w + S_o \mathbf{e}_o + S_g \mathbf{e}_g = S_X \mathbf{e}_X + S_Y \mathbf{e}_Y + S_Z \mathbf{e}_Z, \quad (\text{A.1})$$

may be expressed either in the cartesian axes $(\mathbf{e}_w, \mathbf{e}_o, \mathbf{e}_g)$ or in the cartesian axes $(\mathbf{e}_X, \mathbf{e}_Y)$ in the plane of the triangle \mathcal{T} , and \mathbf{e}_Z out of plane:

$$\begin{aligned} e_X &= \frac{1}{\sqrt{2}}(-e_w + e_o); & e_Y &= \frac{1}{\sqrt{6}}(-e_w - e_o + 2e_g); & e_Z &= \frac{1}{\sqrt{3}}(e_w + e_o + e_g); \\ e_w &= -\frac{e_X}{\sqrt{2}} - \frac{e_Y}{\sqrt{6}} + \frac{e_Z}{\sqrt{3}}; & e_o &= \frac{e_X}{\sqrt{2}} - \frac{e_Y}{\sqrt{6}} + \frac{e_Z}{\sqrt{3}}; & e_g &= \frac{\sqrt{2}}{\sqrt{3}}e_Y + \frac{e_Z}{\sqrt{3}}. \end{aligned} \quad (\text{A.2})$$

The following relations switch from the (X, Y) saturations to the three-phase saturations (and conversely):

$$\begin{aligned} S_X &= \frac{1}{\sqrt{2}}(-S_w + S_o); & S_Y &= \frac{1}{\sqrt{6}}(-S_w - S_o + 2S_g); & S_Z &= \frac{S_w + S_o + S_g}{\sqrt{3}}; \\ S_w &= -\frac{S_X}{\sqrt{2}} - \frac{S_Y}{\sqrt{6}} + \frac{S_Z}{\sqrt{3}}; & S_o &= \frac{S_X}{\sqrt{2}} - \frac{S_Y}{\sqrt{6}} + \frac{S_Z}{\sqrt{3}}; & S_g &= 2\frac{S_Y}{\sqrt{6}} + \frac{S_Z}{\sqrt{3}}. \end{aligned} \quad (\text{A.3})$$

These relations hold for an arbitrary vector: the fact that the three components sum to 1 is not considered.

The effective saturations express in terms of the coordinates of an arbitrary point $\mathbf{M} = (M_X, M_Y)$ of the saturation triangle:

$$\begin{aligned} \underline{S}_w &= \frac{|\mathbf{JK} \wedge \mathbf{JM}|}{|\mathbf{JK} \wedge \mathbf{JI}|} = \frac{1}{2T_r} \left((JK)_X (M_Y - J_Y) - (JK)_Y (M_X - J_X) \right) \\ \frac{d\underline{S}_w}{dS_w} &= \frac{1}{2T_r} \left(-(JK)_X \frac{\sqrt{3}}{\sqrt{2}} + \frac{1}{\sqrt{2}} (JK)_Y \right); & \frac{d\underline{S}_w}{dS_o} &= \frac{1}{2T_r} \left(-(JK)_X \frac{\sqrt{3}}{\sqrt{2}} - \frac{1}{\sqrt{2}} (JK)_Y \right), \\ \underline{S}_o &= \frac{|\mathbf{IM} \wedge \mathbf{IK}|}{|\mathbf{IJ} \wedge \mathbf{IK}|} = \frac{1}{2T_r} \left((M_X - I_X) (IK)_Y - (M_Y - I_Y) (IK)_X \right), \\ \frac{d\underline{S}_o}{dS_w} &= \frac{1}{2T_r} \left(-\frac{(IK)_Y}{\sqrt{2}} + \frac{\sqrt{3}}{\sqrt{2}} (IK)_X \right); & \frac{d\underline{S}_o}{dS_o} &= \frac{1}{2T_r} \left(\frac{(IK)_Y}{\sqrt{2}} + \frac{\sqrt{3}}{\sqrt{2}} (IK)_X \right), \\ \underline{S}_g &= \frac{|\mathbf{IJ} \wedge \mathbf{IM}|}{|\mathbf{IJ} \wedge \mathbf{IK}|} = \frac{1}{2T_r} \left((IJ)_X (M_Y - I_Y) - (IJ)_Y (M_X - I_X) \right), \\ \frac{d\underline{S}_g}{dS_w} &= \frac{1}{2T_r} \left(-(IJ)_X \frac{\sqrt{3}}{\sqrt{2}} + \frac{1}{\sqrt{2}} (IJ)_Y \right); & \frac{d\underline{S}_g}{dS_o} &= \frac{1}{2T_r} \left(-(IJ)_X \frac{\sqrt{3}}{\sqrt{2}} - \frac{1}{\sqrt{2}} (IJ)_Y \right), \end{aligned} \quad (\text{A.4})$$

where $T_r = \frac{1}{2} |\mathbf{JK} \wedge \mathbf{JI}|$ is the area of the irreducible triangle. To calculate the derivatives, the saturations S_w and S_o have been assumed to be the independent variables while $S_g = 1 - S_w - S_o$, and then:

$$M_X = \frac{1}{\sqrt{2}}(-S_w + S_o), \quad M_Y = \frac{1}{\sqrt{6}}(-3S_w - 3S_o + 2). \quad (\text{A.5})$$

Appendix B: First order derivatives of saturations with respect to pressures

To avoid issues with dependent variables, the two effective saturations ($\underline{S}_w, \underline{S}_o$) are taken as independent variables, which simply amount to replace \underline{S}_g by $1 - \underline{S}_w - \underline{S}_o$. The starting point is the knowledge of two capillary relations,

$$p_o - p_w = p_{cow}(\underline{S}_w, \underline{S}_o); \quad p_g - p_o = p_{cgo}(\underline{S}_w, \underline{S}_o). \quad (\text{B.1})$$

These relations are differentiated,

$$dp_o - dp_w = \overbrace{\frac{\partial p_{cow}}{\partial \underline{S}_w}}^{A_{11}} d\underline{S}_w + \overbrace{\frac{\partial p_{cow}}{\partial \underline{S}_o}}^{A_{12}} d\underline{S}_o; \quad dp_g - dp_o = \overbrace{\frac{\partial p_{cgo}}{\partial \underline{S}_w}}^{A_{21}} d\underline{S}_w + \overbrace{\frac{\partial p_{cgo}}{\partial \underline{S}_o}}^{A_{22}} d\underline{S}_o, \quad (\text{B.2})$$

and the result is inverted,

$$\det \mathbf{A} \begin{bmatrix} d\underline{S}_w \\ d\underline{S}_o \end{bmatrix} = \begin{bmatrix} A_{22} & -A_{12} \\ -A_{21} & A_{11} \end{bmatrix} \begin{bmatrix} dp_o - dp_w \\ dp_g - dp_o \end{bmatrix} = \begin{bmatrix} -A_{22} dp_w + (A_{12} + A_{22}) dp_o - A_{12} dp_g \\ A_{21} dp_w - (A_{11} + A_{21}) dp_o + A_{11} dp_g \end{bmatrix}, \quad (\text{B.3})$$

where $\det \mathbf{A} = A_{11} A_{22} - A_{12} A_{21}$. These relations provide the derivatives of the effective saturations, namely for $i = w, o$, $j = w, o, g$,

$$\underline{\mathbf{X}} = [X_{ij}] = \left[\frac{d\underline{S}_i}{dp_j} \right] = \frac{1}{\det \mathbf{A}} \begin{bmatrix} -A_{22} & A_{12} + A_{22} & -A_{12} \\ A_{21} & -(A_{11} + A_{21}) & A_{11} \end{bmatrix}, \quad (\text{B.4})$$

as well as the derivatives of the saturations,

$$\mathbf{X} = [X_{ij}] = \left[\frac{dS_i}{dp_j} \right] = \frac{d\underline{\mathbf{S}}}{d\underline{\mathbf{p}}} = \frac{d\underline{\mathbf{S}}}{d\underline{\mathbf{p}}} \underline{\mathbf{X}}; \quad dS_g = -dS_w - dS_o. \quad (\text{B.5})$$

The 2×2 matrix $d\underline{\mathbf{S}}/d\underline{\mathbf{p}}$ is obtained by expressing the effective saturations in the axes (X, Y) shown in Fig. A.1: it can be extracted from the relations (A.4). The 2×2 matrix $d\underline{\mathbf{S}}/d\underline{\mathbf{S}}$ required in (B.5) is deduced by inversion.

For the capillary pressures (4.4), the coefficients of the matrix \mathbf{A} in (B.2) are identified from the differentials,

$$\begin{aligned} dp_o - dp_w &= \left[30 f(1 - \underline{S}_o) \underline{S}_o + 100 f'(\underline{S}_w) \underline{S}_o \right] d\underline{S}_w \\ &+ \left[-30 f'(1 - \underline{S}_o) c + 30 f(1 - \underline{S}_o) (\underline{S}_o - \underline{S}_g) + 100 f(\underline{S}_w) \right] d\underline{S}_o; \\ dp_g - dp_o &= \left[40 f'(1 - \underline{S}_g) a - 40 f(1 - \underline{S}_g) \times 0.025 \times (1 - \underline{S}_w)^{-0.9} + 30 f(1 - \underline{S}_o) (1 - \underline{S}_o) \right] d\underline{S}_w \\ &+ \left[40 f'(1 - \underline{S}_g) a - 40 f(1 - \underline{S}_g) + 30 f'(1 - \underline{S}_o) b + 30 f(1 - \underline{S}_o) (1 - \underline{S}_o + \underline{S}_g) \right] d\underline{S}_o, \end{aligned} \quad (\text{B.6})$$

where f is the van Genuchten function defined by (4.1) and $f'(x)$ denotes the derivative of f with respect to its argument, i.e. $df = f' dx$,

$$f(\underline{S}) = \left(\underline{S}^{\frac{-1}{m}} - 1 \right)^{\frac{1}{n}}, \quad f' = \frac{df}{d\underline{S}} = -\frac{1}{m n} \left(\underline{S}^{\frac{-1}{m}} - 1 \right)^{-m} \underline{S}^{\frac{-1}{m}-1}, \quad (\text{B.7})$$

where $m = 1 - 1/n$.